

ANALYSIS OF CRACKED BODY REPAIRED BY ADHESIVELY BONDED PATCHES BY BEM-
FEM COUPLING



A Thesis Submitted in Partial Fulfillment of the Requirements
for the Degree of Master of Engineering in Civil Engineering

Department of Civil Engineering

Faculty of Engineering

Chulalongkorn University

Academic Year 2018

Copyright of Chulalongkorn University

การวิเคราะห์วัตถุที่มีรอยร้าวซ่อมแซมด้วยแผ่นประกบโดยระเบียบวิธีร่วมระหว่างระเบียบวิธีบาวดารี
เอลิเมนต์และระเบียบวิธีไฟไนต์เอลิเมนต์



วิทยานิพนธ์นี้เป็นส่วนหนึ่งของการศึกษาตามหลักสูตรปริญญาวิศวกรรมศาสตรมหาบัณฑิต
สาขาวิชาวิศวกรรมโยธา ภาควิชาวิศวกรรมโยธา
คณะวิศวกรรมศาสตร์ จุฬาลงกรณ์มหาวิทยาลัย
ปีการศึกษา 2561
ลิขสิทธิ์ของจุฬาลงกรณ์มหาวิทยาลัย

Thesis Title ANALYSIS OF CRACKED BODY REPAIRED BY ADHESIVELY B
ONDED PATCHES BY BEM-FEM COUPLING
By Mr. Binh Viet Pham
Field of Study Civil Engineering
Thesis Advisor Associate Professor Jaroon Rungamornrat, Ph.D.
Thesis Co Advisor Thai Binh Nguyen, Ph.D.

Accepted by the Faculty of Engineering, Chulalongkorn University in Partial
Fulfillment of the Requirement for the Master of Engineering

..... Dean of the Faculty of Engineering
(Professor Supot Teachavorasinskun, D.Eng.)

THESIS COMMITTEE

..... Chairman
(Professor Teerapong Senjuntichai, Ph.D.)

..... Thesis Advisor
(Associate Professor Jaroon Rungamornrat, Ph.D.)

..... Thesis Co-Advisor
(Thai Binh Nguyen, Ph.D.)

..... Examiner
(Associate Professor Akhrawat Lenwari, Ph.D.)

..... External Examiner
(Weeraporn Phongtinnaboot, Ph.D.)

บิน เวียต แพม : การวิเคราะห์วัตถุที่มีรอยร้าวซ่อมแซมด้วยแผ่นประกบโดยระเบียบวิธี
ร่วมระหว่างระเบียบวิธีบาวดารีเอลิเมนต์และระเบียบวิธีไฟไนต์เอลิเมนต์. (

ANALYSIS OF CRACKED BODY REPAIRED BY ADHESIVELY BONDED PATCHES
BY BEM-FEM COUPLING) อ.ที่ปรึกษาหลัก : จรุงญ รุ่งอมรรัตน์, อ.ที่ปรึกษาร่วม : ไทย
บินท์ เหงียน

วิทยานิพนธ์นี้นำเสนอระเบียบวิธีเชิงตัวเลขที่มีประสิทธิภาพซึ่งมีความสามารถในการ
วิเคราะห์หน่วยแรงในวัตถุสามมิติที่มีรอยร้าวและถูกเสริมกำลังหรือซ่อมแซมด้วยแผ่นการยึดด้วย
ประกบ ระเบียบวิธีที่นำเสนอขึ้นพัฒนาขึ้นภายใต้กรอบของระเบียบวิธีผสมระหว่างระเบียบวิธี
สมการปริพันธ์ขอบและระเบียบวิธีไฟไนต์เอลิเมนต์แบบมาตรฐาน โดยระเบียบวิธีแรกนั้น
ประยุกต์ใช้ในการจัดการกับส่วนของวัตถุที่ยึดหยุ่นที่มีรอยร้าวส่วนระเบียบวิธีที่สองนั้นนำมา
ประยุกต์ใช้จัดการกับแผ่นประกบและชั้นกาว การประมาณการขจัดสัมพัทธ์ที่ผิวรอยร้าวบริเวณ
ใกล้กับขอบรอยร้าวทำให้ถูกต้องมากขึ้นโดยให้ฟังก์ชันฐานเฉพาะที่สามารถจับพฤติกรรมสิ้นสุดได้
อย่างถูกต้อง นอกจากนี้ยังช่วยให้สามารถคำนวณตัวประกอบความเข้มของความเค้นในรูปของ
ข้อมูลที่จุดต่อตามแนวขอบรอยร้าวอีกด้วย มีการนำเสนอผลการวิเคราะห์เพื่อแสดงให้เห็นถึงความ
ถูกต้องและการลู่เข้าของผลเฉลยสำหรับระเบียบวิธีที่พัฒนาขึ้น พร้อมทั้งแสดงให้เห็นถึงอิทธิพล
ของความแข็งแรงสัมพัทธ์ของแผ่นประกบและชั้นกาวที่มีต่อการลดลงของค่าตัวประกอบความ
เข้มของความเค้นตามแนวขอบรอยร้าว

จุฬาลงกรณ์มหาวิทยาลัย
CHULALONGKORN UNIVERSITY

สาขาวิชา วิศวกรรมโยธา

ปีการศึกษา 2561

ลายมือชื่อนิสิต

ลายมือชื่อ อ.ที่ปรึกษาหลัก

ลายมือชื่อ อ.ที่ปรึกษาร่วม

6070236021 : MAJOR CIVIL ENGINEERING

KEYWORD: Boundary integral equation method/ Bonded patches/ Cracked body/ Finite element method/ Stress intensity factors

Binh Viet Pham :

ANALYSIS OF CRACKED BODY REPAIRED BY ADHESIVELY BONDED PATCHES BY BEM-FEM COUPLING. Advisor: Assoc. Prof. Jaroon Rungamornrat, Ph.D. Co-advisor: Thai Binh Nguyen, Ph.D.

This thesis presents an efficient numerical technique capable of handling the stress analysis of three-dimensional cracked bodies strengthened or repaired by adhesively bonded patches. The proposed technique is implemented within the framework of the coupling of the weakly singular boundary integral equation method and the standard finite element procedure. The former is applied to efficiently treat the elastic body containing cracks whereas the latter is adopted to handle both the adhesive layers and the patches. The approximation of the near-front relative crack-face displacement is enhanced by using local interpolation functions that can capture the right asymptotic behaviour. This also offers the direct calculation of the stress intensity factors along the crack front in terms of solved nodal data. A selected set of results is reported to demonstrate the accuracy and convergence of the proposed technique and the influence of relative stiffness of the patches and adhesive layers on the reduction of the stress intensity factor along the crack front.

Field of Study: Civil Engineering

Academic Year: 2018

Student's Signature

Advisor's Signature

Co-advisor's Signature

ACKNOWLEDGEMENTS

I would like to express my deep gratitude to my advisor, Associate Professor Dr. Jaron Rungamornrat, and my co-advisor, Dr. Thai Binh Nguyen, for their assistance throughout research process. They always give me advices and suggestions so that I can complete definitely my research. In addition, I greatly appreciate my committee members due to their supports. Especially, Thanks to kindly assistance provided by the JICA Project for AUN/SEED-Net, I get many chances to not only implement the research effortlessly but also achieve high-quality results in this research. Finally, I want to show my appreciation to my friends, faculty members who aids me to carry out this research.

Binh Viet Pham



TABLE OF CONTENTS

	Page
ABSTRACT (THAI).....	iii
ABSTRACT (ENGLISH).....	iv
ACKNOWLEDGEMENTS	v
TABLE OF CONTENTS	vi
LIST OF FIGURES	1
LIST OF TABLES	5
LIST OF ABBREVIATIONS	6
CHAPTER 1 INTRODUCTION	7
1.1 MOTIVATION AND SIGNIFICANCE.....	7
1.2 BACKGROUND AND REVIEW.....	11
1.3 RESEARCH OBJECTIVE	16
1.4 SCOPE OF WORK	16
1.5 METHODOLOGY AND PROCEDURE.....	16
1.6 OUTCOME AND CONTRIBUTION	18
CHAPTER 2 PROBLEM FORMULATION.....	20
2.1 PROBLEM DESCRIPTION.....	20
2.2 DOMAIN DECOMPOSITION	21
2.3 GOVERNING EQUATIONS FOR PATCHES	23
2.4 GOVERNING EQUATIONS FOR ADHESIVES.....	25
2.5 GOVERNING EQUATIONS FOR CRACKED BODY	27
2.6 GOVERNING EQUATIONS FOR ENTIRE SYSTEM.....	31

CHAPTER 3 SOLUTION PROCEDURE	33
3.1 SOLUTION DISCRETIZATION.....	33
3.2 DISCRETIZED FORM OF GOVERNING EQUATIONS.....	36
3.3 POST-PROCESS FOR STRESS INTENSITY FACTORS	38
CHAPTER 4 NUMERICAL RESULTS AND DISCUSSIONS.....	40
4.1 VERIFICATIONS.....	40
4.1.1 Strengthening of cube containing near surface crack	40
4.1.2 Plate containing centered through crack.....	45
4.1.3 Plate containing surface-breaking semi-elliptical crack	49
4.1.4 Edge cracked bar.....	52
4.2 PARAMETRIC STUDY	56
4.2.1 Plate containing centered through crack.....	56
4.2.2 Plate containing surface-breaking semi-elliptical crack	61
4.2.3 Edge cracked bar.....	64
CHAPTER 5 CONCLUSIONS AND REMARKS.....	67
REFERENCES	69
VITA.....	74

LIST OF FIGURES

Figure 1.1 Full girder depth fatigue crack of Lafayette Street Bridge in St. Paul, MN (Dexter and Ocel, 2013).....	8
Figure 1.2 Cracking in the web gap at a tie girder/floor beam connection on Birmingham Bridge in Pittsburgh, Pennsylvania (Dexter and Ocel, 2013).....	8
Figure 1.3 Repairing cracked steel structures with FRP patches - The Sauvie Island bridge, Portland, Oregon, USA; Mosallam et al. (2013)	9
Figure 2.1 Schematic of a cracked body reinforced by adhesively bonded patches. .	20
Figure 2.2 Schematic of a repaired cracked body separated into three parts: (a) patches, (b) adhesive layers, and (c) cracked body	22
Figure 2.3 Schematic of (a) a generic patch in local coordinate system, (b) patch under the action in \bar{x}_1 direction, and (c) patch under the action in \bar{x}_2 direction.....	24
Figure 2.4 Schematic of (a) a generic adhesive layer in local coordinate system, (b) adhesive layer under the action in \bar{x}_1 direction, and (c) adhesive layer under the action in \bar{x}_2 direction.....	26
Figure 3.1. Local Cartesian coordinate system and parameters essential for determining stress intensity factors along crack front.	39
Figure 4.1. A cube containing near-surface penny-shaped crack strengthened by adhesively bonded patch.	41
Figure 4.2. Three meshes used in numerical simulations (only mesh of each face of cube is shown and it is identical to those for patch and adhesive layer).	42
Figure 4.3. Three meshes adopted to investigate convergence of finite element solutions: Mesh-1 containing 6,930 elements, Mesh-2 containing 13,982 elements, and Mesh-3 containing 43,400-elements.....	43
Figure 4.4. Normalized mode-I stress intensity factor of a near-surface penny-shaped crack embedded in a cube which is subjected to normal traction σ_0 . Results are	

generated by a reliable finite element program and those associated with the case of strengthening are reported for $h^a / w = 0.001$ and $h_p / w = 0.01$	44
Figure 4.5. Normalized mode-I stress intensity factor of a near-surface penny-shaped crack embedded in a cube which is subjected to normal traction σ_0 . Results for the case of strengthening are reported for $h^a / w = 0.001$ and $h_p / w = 0.01$	45
Figure 4.6. Schematic of rectangular plate containing centered through crack and repaired by a pair of adhesively bonded patches.....	46
Figure 4.7. Three meshes adopted in analysis. Meshes of crack are shown below those of boundary.....	47
Figure 4.8. A final mesh (containing 51,450 elements) used to generate converged finite element solution. Mesh is shown only for a quarter of the whole cracked body.	47
Figure 4.9. Normalized mode-I stress intensity factor for a rectangular plate containing centered through crack under normal traction σ_0 with and without repair.	48
Figure 4.10. Schematic of rectangular plate containing surface-breaking, semi-elliptical crack and repaired by adhesively bonded patch.	49
Figure 4.11. Three meshes adopted in the analysis of a rectangular plate containing surface-breaking, semi-elliptical crack. The entire crack mesh and only one quarter of the outer boundary mesh are shown.	50
Figure 4.12. A final mesh (containing 62,510 elements) used to generate converged finite element solution. Mesh is shown only for a quarter of the whole cracked body.	51
Figure 4.13. Normalized mode-I stress intensity factors for rectangular plate containing surface-breaking, semi-elliptical crack under normal traction σ_0	52
Figure 4.14. Schematic of a rectangular bar containing a through-the-thickness, surface-breaking crack under uniformly distributed normal traction and repaired by adhesively bonded patches.	53

Figure 4.15. Three meshes for rectangular bar containing a through-the-thickness, surface-breaking crack. Mesh for the crack mesh is shown below that of the boundary.	54
Figure 4.16. A final mesh (containing 48,840 elements) used to generate converged finite element solution. Mesh is shown only for a quarter of the whole cracked body.	54
Figure 4.17. Normalized mode-I stress intensity factor for rectangular bar containing through-the-thickness, surface-breaking crack under uniformly distributed normal traction σ_0	55
Figure 4.18. Normalized mode-I stress intensity factors along the crack front for plate containing centered through crack after repaired by four different types of patches.	57
Figure 4.19. Percent reduction of mode-I stress intensity factor relative to unrepaired case at four selected points with $s/t \in \{0, 0.3, 0.6, 0.9\}$ versus normalized stiffness of the patch.	59
Figure 4.20. Percent reduction of mode-I stress intensity factor relative to unrepaired case at four selected points with $s/t \in \{0, 0.3, 0.6, 0.9\}$ versus normalized stiffness of the adhesive layer.	61
Figure 4.21. Normalized mode-I stress intensity factors along the crack front for plate containing surface-breaking semi-elliptical crack after repaired by four different types of patches.	62
Figure 4.22. Percent reduction of mode-I SIF relative to unrepaired case at four selected points with $\theta \in \{6.5, 45, 70, 90\}$ versus normalized stiffness of the patch.	63
Figure 4.23. Percent reduction of mode-I SIF relative to unrepaired case at four selected points with $\theta \in \{6.5, 45, 70, 90\}$ versus normalized stiffness of adhesive layer.	63
Figure 4.24. Normalized mode-I SIF along the crack front for edge cracked bar after repaired by four different types of patches.	65

Figure 4.25. Percent reduction of mode-I SIF from unrepaired case at four selected points with $s/t \in \{0, 0.25, 0.6, 0.967\}$ versus normalized stiffness of the patch..... 65

Figure 4.26. Percent reduction of mode-I SIF from unrepaired case at four selected points with $s/t \in \{0, 0.25, 0.6, 0.967\}$ versus normalized stiffness of adhesive layer. 66



LIST OF TABLES

Table 4.1. Material properties for cracked body, patch, and adhesive layer	41
Table 4.2. Material properties for different types of patches (e.g., Liu and Xu, 2000; Jiann-Quo and Kam-Lun, 1991; Yu et al., 2014).....	57
Table 4.3. Material properties for different types of adhesive layers (e.g., Ricci et al., 2011; Rodríguez-Tembleque and Aliabadi, 2016)	60



LIST OF ABBREVIATIONS

U_j^p	kernel in boundary integral equations
C_{mj}^{tk}	kernel in boundary integral equations
G_{mj}^p	kernel in boundary integral equations
H_{ij}^p	kernel in boundary integral equations
S_0	ordinary boundary of the cracked body
S_u	surface which the displacement is prescribed
S_t	surface which the traction is prescribed
S_c^+, S_c^-	crack surfaces
S_a	surface which the patch is attached
h_p	thickness of the patch
h^a	thickness of the adhesive layer
$\bar{\mathbf{u}}^{*p}$	in-plane displacement within the patch
$\bar{\boldsymbol{\sigma}}^{*p}$	in-plane stress within the patch
$\bar{\boldsymbol{\varepsilon}}^{*p}$	in-plane strain within the patch
\mathbf{C}^{*p}	elastic in-plane modulus matrix for the plane-stress case
G^a	elastic shear modulus of the adhesive material
$\bar{\boldsymbol{\sigma}}^{*a}$	out-of-plane shear stress within the layer
n_i	components of the outward unit normal vector
D_m	surface differential operator
\mathbf{t}^{bu}	unknown traction on the surface S_u
\mathbf{u}^{bt}	unknown displacement on the surface S_t
$\Delta \mathbf{u}^b$	unknown relative crack-face displacement
\mathbf{u}^{ba}	unknown displacement on the surface S_a
E_{nijpn}	elastic moduli of the material constituting the cracked body
\mathbf{T}	standard transformation matrix

CHAPTER 1

INTRODUCTION

This chapter begins with outlining the motivation of the present research and its significance. Then, results from an extensive literature survey are briefly presented not only to identify the existing gap of knowledge but also to support the novel aspect of the proposed work. A clear objective, scope of work, research procedure and essential methodology are, subsequently, summarized to demonstrate the solid framework of the present research. Finally, outcomes and contributions to related communities are addressed.

1.1 MOTIVATION AND SIGNIFICANCE

Sustainability and integrity of engineering structures are ones among various crucial issues that must be properly integrated in the design procedure and the subsequent maintenance stage. It has been known that the presence of cracks/flaws/damages is one of the major causes of subsequent failures of components, parts of or the entire structures leading finally to the loss of their functions. According to statistics, more than 50% of recorded fracture accidents can be attributed to the fatigue cracking (Sangid, 2013). In general, the cracking failure possesses some inherent characteristics such as complexity, suddenness, and repeatability (Zhu et al., 2016). In particular, existing cracks can advance dramatically on the surface of structural components under the influences of both applied loadings and undesirable environmental conditions, and this may lead to catastrophic failures (see Figure 1.1 and Figure 1.2 for examples of cracks induced within structural components such as girders of steel bridges). For such reason, the repair of damaged/cracked structures at the earliest time as soon as they are detected during inspections is considered essential. Furthermore, the control of cracked structures after being repaired is also one of vital tasks to evaluate the selected repairing method so that those repaired structures can maintain their bearing capacity.



Figure 1.1 Full girder depth fatigue crack of Lafayette Street Bridge in St. Paul, MN (Dexter and Ocel, 2013).

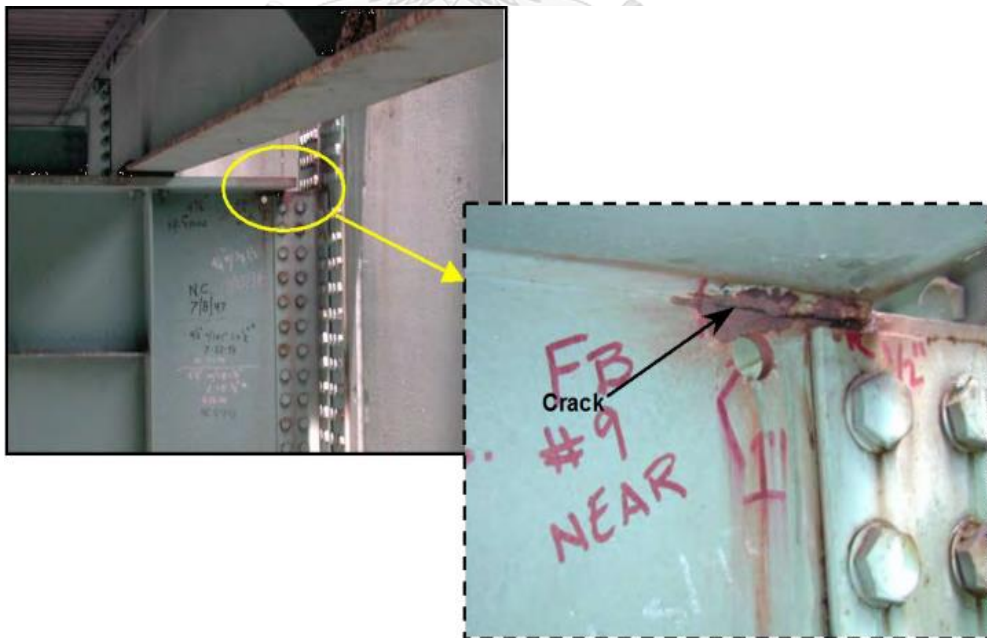


Figure 1.2 Cracking in the web gap at a tie girder/floor beam connection on Birmingham Bridge in Pittsburgh, Pennsylvania (Dexter and Ocel, 2013).

Replacement of (repairable) cracked or damaged parts can be time-consuming and expensive, and, in addition, require a high level of expertise. It is usually more cost effective to repair those damaged components by using patching techniques. One of those methods, with adhesively bonded repairs, has been widely employed in practices (see Figure 1.3 for the installation of patches for repairing a steel bridge). Many theoretical and empirical investigations have demonstrated the advantages of this particular method relative to other existing techniques for repairing cracked structures due mainly to its cost effectiveness (e.g., Arendt and Sun, 1994; Baker, 1988; Jones, 1984; Ratwani, 1977a, 1977b, 1978, 1979; Rose, 1981; Sun et al., 1996; Young et al., 1992). In addition to their high stiffness and strength, the patches are structurally efficient and induce much less damages to the repaired structures.



Figure 1.3 Repairing cracked steel structures with FRP patches - The Sauvie Island bridge, Portland, Oregon, USA; Mosallam et al. (2013)

In the modeling point of view via a theory of linear elasticity and linear elastic fracture mechanics, the stress intensity factor along the crack front can be

significantly reduced after the cracked body is repaired by attaching a patch over the cracked region (e.g., Alaimo et al., 2009; Jiann-Quo and Kam-Lun, 1991; Liu et al., 2009; Pisa and Aliabadi, 2015; Salgado and Aliabadi, 1996, 1998; Sekine et al., 2005; Useche et al., 2008; Wen et al., 2000, 2002, 2003; Widagdo and Aliabadi, 2001; Young et al., 1992; Yu et al., 2014). This is due to the fact that some of externally applied loads exerted to the cracked bodies are either shared by or transferred directly to the patch via the adhesive layer rendering the enhancement of stiffness near the patching region and the reduction of relative crack-face displacements. As a direct consequence, the growth of the cracks can be delayed or even ceased if the repair is properly designed. Evidences from past studies have indicated that various parameters including the dimensions and material properties of the repaired structure, the patch, and the adhesive layer significantly affects the efficiency and effectiveness of the repair (e.g., Alaimo et al., 2009; Jiann-Quo and Kam-Lun, 1991; Liu et al., 2009; Pisa and Aliabadi, 2015; Salgado and Aliabadi, 1996, 1998; Sekine et al., 2005; Useche et al., 2008; Wen et al., 2000, 2002, 2003; Widagdo and Aliabadi, 2001; Young et al., 1992; Yu et al., 2014). The full investigation to understand the role of those parameters is considered essential and can assist designers/engineers in the optimization of their designs. While experimental studies offer an excellent means to establish a set of results reflecting real responses, the methods themselves consume a significant amount of resources and are quite limited to test settings. In particular, to assess efficiency and influence of the patches in the experiments, a large set of testing specimens including un-patched and patched cracked structures for various specimen configurations must be considered. An alternative approach is to adopt computer-based simulations, based upon a set of calibrated governing physics and solution procedures, to perform such a parametric study. It is remarked, however, that to accomplish such an important task within a broad and general framework (e.g., three-dimensional settings, large-scale and complex cases), powerful and computationally efficient tools are prerequisite.

1.2 BACKGROUND AND REVIEW

This particular section primarily reports results from the review of literature relevant to the present study not only to display the historical development but also to identify the key gap of knowledge.

Adhesive bonding has been widely used for repairing damaged structures in practices. In particular, the repair of cracked bodies by bonding patches is considered as a fundamental issue in assessing the efficiency and the feasibility of such the repair. Evaluation of the stress intensity factors at the crack front and the stress transferred by the adhesive layer is considered vital in identifying the critical parameters for the crack patching design. Jiann-Quo and Kam-Lun (1991) analyzed a two-dimensional problem for cracked plates with a bonded patch by using a coupling technique between the boundary integral equation method and a standard finite element technique. In their study, a shear spring model was adopted to represent the effect of the adhesive layer whereas the patch was treated by the finite element technique and the cracked plate was analyzed by the boundary integral equation method. Their results implied that the thickness of the patches has the significant influence on the stress intensity factors at the crack tips and also demonstrate the important role of the patch material. Later, Young et al. (1992) applied a similar approach together with the compatibility of the deformation to analyze the stress distribution in cracked finite sheets symmetrically reinforced by bonded patches and stiffeners. The influence of reinforcements was considered as a distribution of forces over the attachment regions. An adhesive layer was assumed to resist only the shear stresses where other stress components were ignored in the loading transfer. In addition, the geometry used in simulations was limited to cases where the crack is completely described by a single straight line.

To solve the problem with any number of edged and embedded cracks in any given geometry, Salgado and Aliabadi (1996) proposed the dual boundary element method (DBEM) for modeling cracked stiffened panels. In the analysis, the displacement compatibility between the thin sheet and the stiffeners was enforced and the J-integral technique was applied to determine the stress intensity factors.

The DBEM was also extended to simulate multiple crack advances in stiffened panels by using Paris law. They also concluded that the implemented technique yields accurate results and have been successfully applied to model a wide range of problems. Later, Salgado and Aliabadi (1998) developed a formulation based on the DBEM and the dual reciprocity method (DRM) for the analysis of thin cracked metal sheets which were adhesively bonded by thin metal patches and stiffeners. The stiffened cracked sheet was modeled by the DBEM to overcome difficulties associated with the modeling of cracks. Any number of edged and embedded cracks and straight with and without kinks can be handled. Adhesive shear stresses were considered as the action-reaction body forces exchanged by the sheet and the patches. The DRM was adopted to avoid the discretization of the patch attachment domain into a collection of internal cells. The J-integral technique was employed to determine the stress intensity factors. Wen et al. (2000) later modeled a two-dimensional, stiffened plate containing cracks and subjected to uniform distributed moment on the crack surface and uniform shear load on the plate using the coupling boundary element formulation of shear deformable plate and two dimensional plane stress elasticity. The interaction forces along the attachment (or the interface) between the stiffeners and the plate were treated as the line distributed body forces. The stress intensity factors for both the bending and in-plane loading cases were obtained from the crack opening displacement data.

The application of two-dimensional boundary element method to the analysis of cracked panels repaired by mechanically fastened composite patches can be found in the work of Widagdo and Aliabadi (2001). Mechanically fastened composite patches were often used in special cases for the repair of thick panels and where the control for repairing the adhesive patch was unavailable. In their analysis, mechanical fasteners were modeled as linear springs whose forces were treated as concentrated forces. In addition, special crack-tip shape functions were employed to approximate the near-tip fields whereas the crack-opening displacement data were utilized in the post-process for the stress intensity factors. While the analysis procedure based upon the boundary element method such as those proposed by Young et al. (1992) and Salgado and Aliabadi (1998) have been

found versatile and yielding accurate results in the modeling of repaired panels, the developments were carried out within the context of two-dimensional setting and the bending effect caused by adhesive patches was not considered.

The integration of the bending effect of patches via Mindlin plate theory was carried out later in the work of Wen et al. (2002). In their study, the flat cracked panels with adhesively bonded patches were analyzed with the interaction between attachment regions being handled as a distribution of in-plane, out-of-plane and two-moment body forces. The boundary integral equations were formulated for the shear deformable plate whereas the governing equations for the patches were obtained based on two-dimensional, plane-stress, linear elasticity. The coupling between the boundary integral equation method and the finite element approximations was adopted in the solution procedure. Their results demonstrated that when the bending effect is taken into account, the maximum stress intensity factor at a surface breaking point rose significantly about three times compared with that given by Young et al. (1992). Wen et al. (2003) further extended the work of Wen et al. (2002) to handle curved cracked panels with adhesively bonded patches. According to their result, the out of plane bending behavior and the panel curvature had the significant influence on the magnitude of the stress intensity factors at the crack tip. The normalized maximum stress intensity factor, attained at the surface breaking point on the patched panel, increases sharply with the increase of panel curvature.

The application of BEM-FEM coupling to investigate the fatigue crack growth of cracked aluminum panels repaired with an adhesively bonded fiber-reinforced polymer (FRP) composite patch was carried out by Sekine et al. (2005). The cracked panel was treated by BEM whereas the FRP composite laminate was modeled by FEM. The adhesive layer was represented by linear springs to connect the panels and the patches. In the simulation of crack advance under the cyclic loading, both the boundary element and finite element meshes were re-constructed in each incremental loading step. The crack-front profiles during the propagation and the distribution of the stress intensity factors along crack fronts were obtained to assess the fatigue crack growth behavior. A series of experiments was also implemented and obtained results were then used to evaluate the validity of the proposed

mathematical model. Later, Useche et al. (2008) applied a similar technique as that used by Wen et al. (2002) to analyze cracked thick plates repaired with adhesively bonded composite patches. In their work, the shear deformable, isotropic cracked plate was modeled by Kirchhoff's plate theory and then solved by the dual boundary integral equation method. The interaction forces and moments at the attachment regions were treated as a distributed body load.

Due to the vast and recent growth of applications of smart materials in engineering applications, active piezoelectric patches were also used in the repair of cracked structures. Alaimo et al. (2009) developed a numerical procedure based mainly on the boundary integral equation method to investigate such situations. Mechanical responses of the repaired structures were examined for both perfect and imperfect interfaces between the patches and the host beams. In the case of an imperfect interface, a spring model was utilized to represent the contribution of the adhesive layer which involves both shear and peeling stiffness and through the assumption that the displacement jump at the interface is proportional to the traction. Based on the piezoelectric effect, the strain induced by an applied electric field across the piezoelectric patch can, in fact, help the structure to reduce the crack opening displacement. Their results also showed that as the adhesive influence became more significant, the applied voltage needed to close the crack mouths, and so to obtain the maximum reduction of the stress intensity factors, increases. In the same year, Liu et al. (2009) employed a numerical software package (i.e., BEASY) to compute the stress intensity factors (SIFs) and study the crack propagation and fatigue lives of the cracked steel plates repaired by carbon fiber reinforced polymer (CFRP). The composite patch and the cracked steel plate were simulated using the surface elements whereas the adhesive layer was treated by interface elements to connect both the patch and the steel plate. A set of experimental results was carried out and then used to validate their model. Results obtained from simulations indicated the significant influences of the bond length, the bond width, the patch configuration, the CFRP layer number, the modulus of the composite patch and the adhesive shear modulus on the stress intensity factors. In particular, as the bond length is less than the optimal value, the fatigue life increases monotonically with

respect to the increase in the bond length. In the contrary, when the bond length exceeded the optimal bond length, no obvious increase in the fatigue life was observed with the increase in the bond length. In the case of crack propagation, the used of wider composite was obviously more efficient in reducing the effective stress intensity factors. Also, increasing the number of CFRP layers was found to significantly reduce the effective stress intensity factors. Later, Yu et al. (2014) also adopted the software BEASY to investigate the effectiveness of CFRP when applied at different stages of crack propagation in steel elements. In their analysis, a numerical study on CFRP retrofitted steel plates with different degrees of damages was carried out by using the boundary element method. Obtained numerical results were found in good agreement with existing experimental data. They also pointed that the boundary element method was a reliable and robust numerical tool for crack propagation analysis of CFRP laminate retrofitted steel plate. In addition, a parametric study was carried out to investigate the influence of the bond length, the bond width, the CFRP stiffness and the adhesive shear modulus on the stress intensity factors and concluding results were consistent with those of Liu et al. (2009). Recently, Pisa and Aliabadi (2015) developed a technique based mainly on a boundary integral equation method to solve a problem associated with stiffened panels with repairing patches. In their study, the BEM formulation was enhanced to allow the treatment of complex structures including all the features of stiffeners and repairing patches. The stiffeners modeled either as intact or broken elements were formulated as an assembled structure using a multi-domain formulation. The repairing patches can be either riveted or adhesively bonded. The crack-opening displacement method and the J-integral-type formula were implemented to assess the required fracture parameters. The rivet load was considered to be uniformly distributed along a line segment, perpendicular to the force and centered at the application point. Their results indicated that solution for the adhesive case was close to the solid model; while the rivet model yields the highest deflection caused by higher loads in the patch and generates higher moments.

It should be remarked that most of studies indicated above were established within the two-dimensional framework and quite specific to certain settings such as

the repair configurations and types of repaired structures. The extension of the existing modeling techniques to be capable of handling more complex and general scenarios such as fully three-dimensional and large scale problems is challenging and requires further extensive investigations. In particular, the enhancement of boundary integral equation methods, together with the finite element procedure, to have the capability to simulate repaired crack structures to the level of complexity involved should be of sufficient merits and offer useful computational tools for performing a comprehensive investigation of the repair performance.

1.3 RESEARCH OBJECTIVE



The proposed research aims to (1) develop a numerical procedure for the analysis of the fracture data along the crack-front of cracked bodies repaired by adhesive patched and (2) investigate the influence of the thickness and modulus of the patches and adhesive layers on the fracture response after the repair.

1.4 SCOPE OF WORK



The research has been carried out within the following framework: (i) a cracked body is finite, three-dimensional and free of body force, contains either embedded or surface breaking cracks, and made of a homogeneous, linear elastic material; (ii) repaired surfaces are flat; (iii) patches are relatively thin with negligible bending effect and made of homogeneous, linear elastic materials; (iv) an adhesive layer can be represented as a shear layer with an infinitesimal thickness; (v) damage and debonding failure of the interface are not included; and (vi) only the stress intensity factors are of interest.

1.5 METHODOLOGY AND PROCEDURE

Fundamental theories, basic assumptions, key methodology and essential research procedures for the current study are briefly summarized below.

- 1) A technique of domain decomposition is adopted to separate a cracked body repaired by adhesive patches into three parts including a cracked body, patches, and adhesive layers.
- 2) Mechanical responses of cracked bodies are modeled by a classical theory of linear elasticity (e.g., Gurtin, 1973; Karasudhi, 2012; Timoshenko and Goodier, 1970). A pair of weakly singular, weak-form boundary integral equations for the displacements and tractions proposed by Rungamornrat and Mear (2008) is used as the basis for the development of the key governing equations. In particular, the displacement boundary integral equation is adopted on a part of the ordinary boundary where the displacement is prescribed whereas the traction boundary integral equation is applied to all crack surfaces, a part of the ordinary boundary where the traction is prescribed, and the repaired surfaces.
- 3) Mechanical responses of patches are modeled by a classical theory of two-dimensional, plane-stress, linear elasticity (e.g., Gurtin, 1973; Karasudhi, 2012; Timoshenko and Goodier, 1970). A standard procedure based on either the principle of virtual work or the weighted residual technique (e.g., Bathe, 2006; Hughes, 2012; Zienkiewicz et al., 2000) is adopted to formulate the governing weak-form equation for each patch.
- 4) Governing differential equations of each adhesive layer are established based on the assumption that the layer thickness is infinitesimal and only shear resistance is considered. A weighted residual technique is then applied to construct the alternative weak-form statement.
- 5) The continuity of displacements and tractions along the interface between the patch and the adhesive layer and that between the cracked body and the adhesive layer is enforced to form a system of equations governing the whole repaired body.
- 6) The weakly singular boundary integral equations for the cracked body are discretized using the concept of symmetric Galerkin boundary element method proposed by Rungamornrat and Mear (2008). A special near-front approximation of the relative crack-face displacement employed by Li et al. (1998) and

Rungamornrat and Mear (2008) are also adopted to enhance the accuracy and computational efficiency.

- 7) Standard finite element procedure (e.g., Bathe, 2006; Hughes, 2012; Zienkiewicz et al., 2000) is adopted to discretize the weak-form equations for both patches and adhesive layers.
- 8) A resulting system of linear algebraic equations involving unknown nodal data on the crack surfaces, the boundary of the cracked body, and on patches is solved using an efficient linear solver.
- 9) The stress intensity factors are post-processed directly from the relative crack-face displacements in the neighborhood of the crack front using the explicit formula proposed by Rungamornrat and Mear (2008). Such algorithm relies upon the use of special crack-tip elements along the crack front with their shape functions properly enriched to include the square-root behavior and the integration of extra degrees of freedom directly related to the stress intensity factors.
- 10) All proposed numerical procedures are implemented in a form of an in-house computer code using standard FORTRAN language.
- 11) An extensive numerical study is carried out to fully investigate the influence of various parameters such as the repair configurations and material properties of both patches and adhesive layers on the performance of the repair.

1.6 OUTCOME AND CONTRIBUTION

One obvious merit of the present study is the offer of a computationally efficient and robust numerical technique capable of performing the full stress analysis of cracked bodies after repaired by adhesive patches. The proposed technique is carried out in a quite common framework which allows to analyze various scenarios applicable to practical applications. The availability of such a high capability computational tool should assist engineers/designers to attain optimal solutions in

the design procedure and also ensure the performance and integrity of damaged components and structures after repaired.



CHAPTER 2

PROBLEM FORMULATION

In this chapter, a brief summary of the problem formulation is presented. The description of the research problem is outlined first and the boundary value problem is then formulated. The domain decomposition technique together with the boundary integral formulation and the weighted residual procedure is adopted to form the entire system of governing equations.

2.1 PROBLEM DESCRIPTION

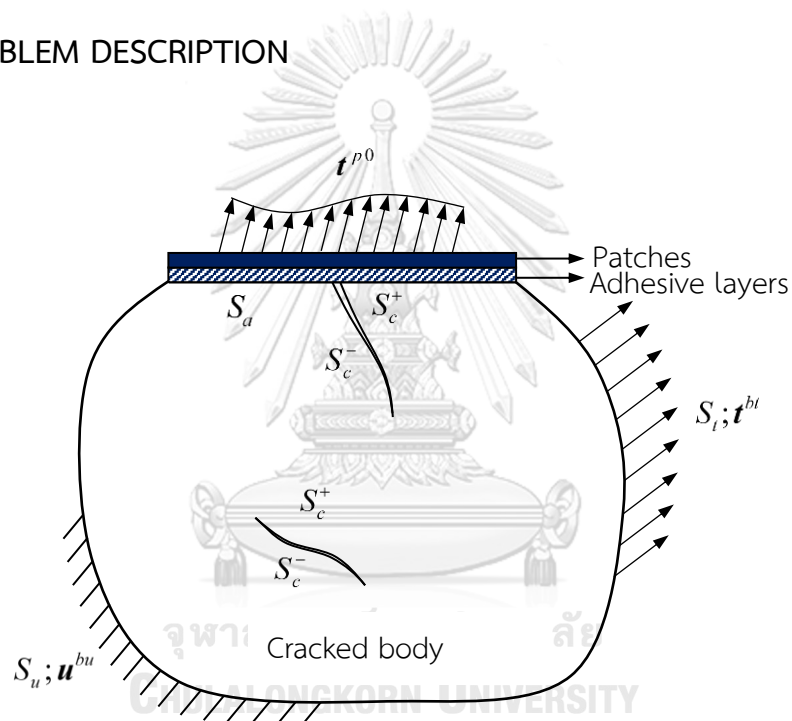


Figure 2.1 Schematic of a cracked body reinforced by adhesively bonded patches.

Consider a three-dimensional, finite body which contains embedded and surface-breaking cracks and is reinforced by adhesively bonded patches as shown schematically in Figure 2.1. The cracked body is made of a homogeneous, generally anisotropic, linear elastic material. The ordinary boundary of the cracked body, denoted by S_0 , consists of a surface S_u on which the displacement \mathbf{u}^{bu} is prescribed, a surface S_t on which the traction \mathbf{t}^{bt} is known, and a flat or planar surface S_a on which the patch is attached. The surface of cracks is represented by a

pair of geometrically identical surfaces, denoted by S_c^+ and S_c^- , and, in the present study, the attention is restricted only to the case that the crack surface is subjected to self-equilibrated tractions; i.e., the tractions $\mathbf{t}^{b+}, \mathbf{t}^{b-}$ acting to the surfaces S_c^+, S_c^- , respectively, satisfy $\mathbf{t}^{b+} + \mathbf{t}^{b-} = \mathbf{0}$. Each patch is of infinitesimal thickness, made of a homogeneous, linear elastic material and fully attached to the cracked body on the surface S_a by means of an adhesive bonding material. The prescribed traction exerted to the surface of the patch, opposite to the attached surface, is denoted by \mathbf{t}^{p0} . In the present study, the thickness of each adhesive layer is assumed small and only the shear resistance is considered.

2.2 DOMAIN DECOMPOSITION

To establish a set of equations governing mechanical responses of the cracked body after repaired with adhesively bonded patches, the medium is first fictitiously separated into three portions: a cracked body Ω , patches Ω_p , and adhesive layers Ω_a as illustrated in Figure 2.2. The shear and normal tractions exerted on the surface S_a of the cracked body by the adhesive layers are denoted by \mathbf{s}^{ba} and \mathbf{q}^{ba} , respectively, whereas the shear and normal tractions exerted on the patches by the adhesive layers are denoted by \mathbf{s}^{pa} and \mathbf{q}^{pa} , respectively. For the adhesive layers, the shear and normal tractions exerted by the cracked body and the patches are denoted by $\{\mathbf{s}^{ab}, \mathbf{q}^{ab}\}$ and $\{\mathbf{s}^{ap}, \mathbf{q}^{ap}\}$, respectively. From the assumption that the bending effect of the patches is negligible, the normal traction \mathbf{q}^{pa} is directly related to the prescribed traction \mathbf{t}^{p0} on the patches by

$$\mathbf{q}^{pa} + (\mathbf{t}^{p0} \cdot \mathbf{n}^p) \mathbf{n}^p = \mathbf{0} \quad (2.1)$$

where \mathbf{n}^p is a unit normal vector to the patches. Similarly, from the assumption that the adhesive layer can take only shear, the normal tractions \mathbf{q}^{ab} and \mathbf{q}^{ap} must be self-equilibrated, i.e.

$$\mathbf{q}^{ab} + \mathbf{q}^{ap} = \mathbf{0} \quad (2.2)$$

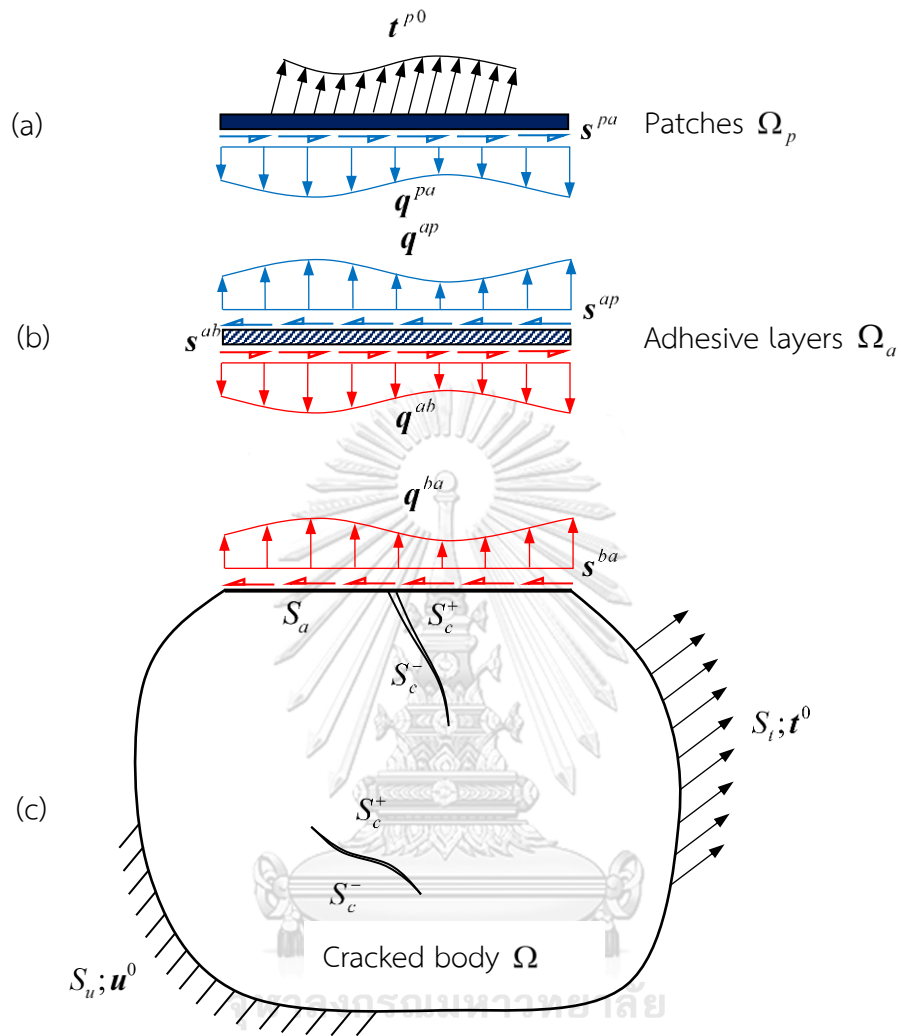


Figure 2.2 Schematic of a repaired cracked body separated into three parts: (a) patches, (b) adhesive layers, and (c) cracked body

From the continuity of the displacements and tractions along the interface between the patches and the adhesive layers, it gives rise to

$$\mathbf{u}^p = \mathbf{u}^{ap} \quad (2.3)$$

$$\mathbf{s}^{pa} + \mathbf{s}^{ap} = \mathbf{0} \quad (2.4)$$

$$\mathbf{q}^{pa} + \mathbf{q}^{ap} = \mathbf{0} \quad (2.5)$$

where \mathbf{u}^p and \mathbf{u}^{ap} present the displacement of the patches, and the adhesive layers along the interface, respectively. Similarly, the continuity of the displacements and tractions along the interface of the cracked body and the adhesive layers leads to the relations

$$\mathbf{u}^{ba} = \mathbf{u}^{ab} \quad (2.6)$$

$$\mathbf{s}^{ba} + \mathbf{s}^{ab} = \mathbf{0} \quad (2.7)$$

$$\mathbf{q}^{ba} + \mathbf{q}^{ab} = \mathbf{0} \quad (2.8)$$

where \mathbf{u}^{ba} and \mathbf{u}^{ab} denote the displacement of the cracked body and the adhesive layers at the interface, respectively. Combining equations (2.1), (2.2), (2.5) and (2.8) yields

$$\mathbf{q}^{ba} = -\mathbf{q}^{ab} = \mathbf{q}^{ap} = -\mathbf{q}^{pa} = (\mathbf{t}^{p0} \cdot \mathbf{n}^p) \mathbf{n}^p \quad (2.9)$$

The relation (2.9) illustrates that the normal component of the prescribed traction \mathbf{t}^{p0} transferred directly to the cracked body and the normal tractions transferred at the two interfaces are known a priori. The latter condition allows ones to drop the normal tractions \mathbf{q}^{pa} and $\mathbf{q}^{ab}, \mathbf{q}^{ap}$ in the formulation of governing equations of the patches and the adhesive layers without loss.

2.3 GOVERNING EQUATIONS FOR PATCHES

Consider a generic two-dimensional patch, denoted by Ω_p , under the action of the prescribed shear traction \mathbf{s}^{p0} (i.e., a tangential component of the prescribed traction \mathbf{t}^{p0}) and the unknown shear traction \mathbf{s}^{pa} exerted by the adhesive layer as illustrated in Figure 2.3. Along the boundary of the patch $\partial\Omega_p$, the traction identically vanishes. For convenience in further analysis of the governing equations for the patch, a local Cartesian coordinate system $\{\mathbf{O}; \bar{x}_1, \bar{x}_2, \bar{x}_3\}$ is introduced such that the \bar{x}_3 axis is normal to the plane of the patch and also directs outward to the cracked body (i.e., has the same direction as the outward unit normal vector to the surface S_p of the cracked body); in particular, the $\bar{x}_1 - \bar{x}_2$ plane is coincident with the plane of the patch.

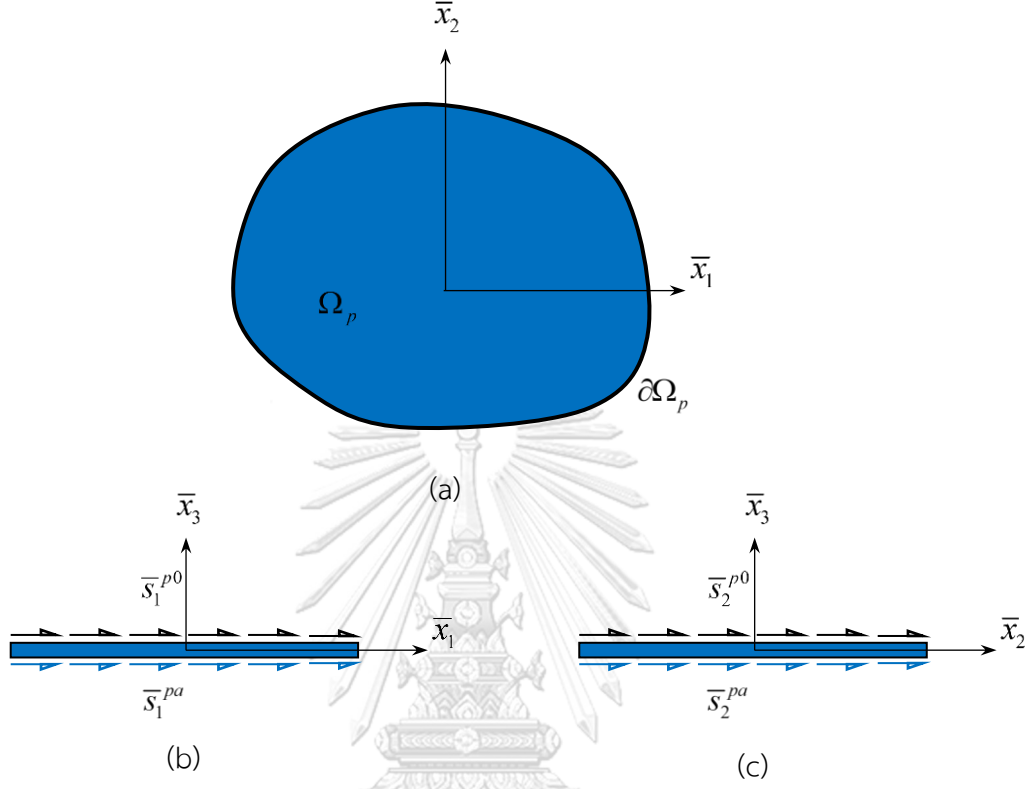


Figure 2.3 Schematic of (a) a generic patch in local coordinate system, (b) patch under the action in \bar{x}_1 direction, and (c) patch under the action in \bar{x}_2 direction.

Since the thickness of the patch is assumed infinitesimal and the bending effect is negligible, its responses can be properly modeled by a two-dimensional, plane-stress, linear elasticity. The in-plane displacement $\bar{\mathbf{u}}^{*p} = \{\bar{u}_1^p \quad \bar{u}_2^p\}^T$, the in-plane stress $\bar{\boldsymbol{\sigma}}^{*p} = \{\bar{\sigma}_{11}^p \quad \bar{\sigma}_{22}^p \quad \bar{\sigma}_{12}^p\}^T$ and the in-plane strain $\bar{\boldsymbol{\epsilon}}^{*p} = \{\bar{\epsilon}_{11}^p \quad \bar{\epsilon}_{22}^p \quad 2\bar{\epsilon}_{12}^p\}^T$ within the patch are related by following field equations

$$h_p \mathbf{L}^T \bar{\boldsymbol{\sigma}}^{*p} + \bar{\mathbf{s}}^{*pa} + \bar{\mathbf{s}}^{*p0} = \mathbf{0} \quad (2.10)$$

$$\bar{\boldsymbol{\sigma}}^{*p} = \mathbf{C}^{*p} \bar{\boldsymbol{\epsilon}}^{*p} \quad (2.11)$$

$$\bar{\boldsymbol{\epsilon}}^{*p} = \mathbf{L} \bar{\mathbf{u}}^{*p} \quad (2.12)$$

where the superscript “ T ” denote the matrix transpose; h_p is the thickness of the patch; $\bar{\mathbf{s}}^{*pa} = \{\bar{s}_1^{pa} \quad \bar{s}_2^{pa}\}$ contains local components of \mathbf{s}^{pa} , $\bar{\mathbf{s}}^{*p0} = \{\bar{s}_1^{p0} \quad \bar{s}_2^{p0}\}$

contains local components of \mathbf{s}^{p0} ; \mathbf{C}^{*p} is the elastic in-plane modulus matrix for the plane-stress case; and \mathbf{L} is the differential operator defined by

$$\mathbf{L} = \begin{bmatrix} \frac{\partial}{\partial \bar{x}_1} & 0 \\ 0 & \frac{\partial}{\partial \bar{x}_2} \\ \frac{\partial}{\partial \bar{x}_2} & \frac{\partial}{\partial \bar{x}_1} \end{bmatrix} \quad (2.13)$$

Combing (2.10) - (2.12) leads to a system of linear, second-order partial differential equations in terms of the in-plane displacement $\bar{\mathbf{u}}^{*p}$:

$$h_p \mathbf{L}^T \mathbf{C}^{*p} \mathbf{L} \bar{\mathbf{u}}^{*p} + \bar{\mathbf{s}}^{*pa} + \bar{\mathbf{s}}^{*p0} = \mathbf{0} \quad (2.14)$$

The weak-form statement of (2.14) can be constructed readily using a standard procedure. In particular, by utilizing the weighted residual technique to (2.14) and then employing the traction-free condition along the boundary of the patch and the integration by parts via Gauss-divergence theorem, it gives rise to

$$\int_{\Omega_p} h_p (\mathbf{L} \bar{\mathbf{w}}^p)^T \mathbf{C}^{*p} \mathbf{L} \bar{\mathbf{u}}^{*p} dA - \int_{\Omega_p} (\bar{\mathbf{w}}^p)^T \bar{\mathbf{s}}^{*pa} dA = \int_{\Omega_p} (\bar{\mathbf{w}}^p)^T \bar{\mathbf{s}}^{*p0} dA \quad (2.15)$$

where $\bar{\mathbf{w}}^p$ denotes any sufficiently smooth test function. The weak-form statement (2.15) form the governing equation for each patch and it contains two unknown functions including the unknown in-plane displacement of each patch $\bar{\mathbf{u}}^{*p}$ and the unknown shear traction $\bar{\mathbf{s}}^{*pa}$ applied to the patch by the adhesive layer.

2.4 GOVERNING EQUATIONS FOR ADHESIVES

Now, consider a generic adhesive layer, denoted by Ω_a , which is subjected to the unknown shear traction \mathbf{s}^{ap} exerted by the patch and the unknown shear traction \mathbf{s}^{ab} exerted by the cracked body as demonstrated in Figure 2.4. The thickness of the adhesive layer is denoted by h^a and the same local coordinate system $\{\mathbf{O}; \bar{x}_1, \bar{x}_2, \bar{x}_3\}$ as that introduced for the patch is also applied here.

From the assumption that the adhesive layer can transfer only shear across its thickness, the state of strain can be completely described by the out-of-plane shear strain components $\bar{\boldsymbol{\varepsilon}}^{*a} = \{\bar{\boldsymbol{\varepsilon}}_{31}^a \quad \bar{\boldsymbol{\varepsilon}}_{32}^a\}^T$. Since the thickness of the adhesive layer is infinitesimal in comparison with its planar dimensions, it is legitimate to assume that the out-of-plane shear strain components are independent of \bar{x}_3 or, equivalently, the in-plane displacements $\bar{\mathbf{u}}^{*a} = \{\bar{u}_1^a \quad \bar{u}_2^a\}^T$ vary linearly across the thickness. As the direct consequence, the strain-displacement relationship for this particular case reduces to

$$\bar{\boldsymbol{\varepsilon}}^{*a} = \frac{1}{h^a} (\bar{\mathbf{u}}^{*ap} - \bar{\mathbf{u}}^{*ab}) \quad (2.16)$$

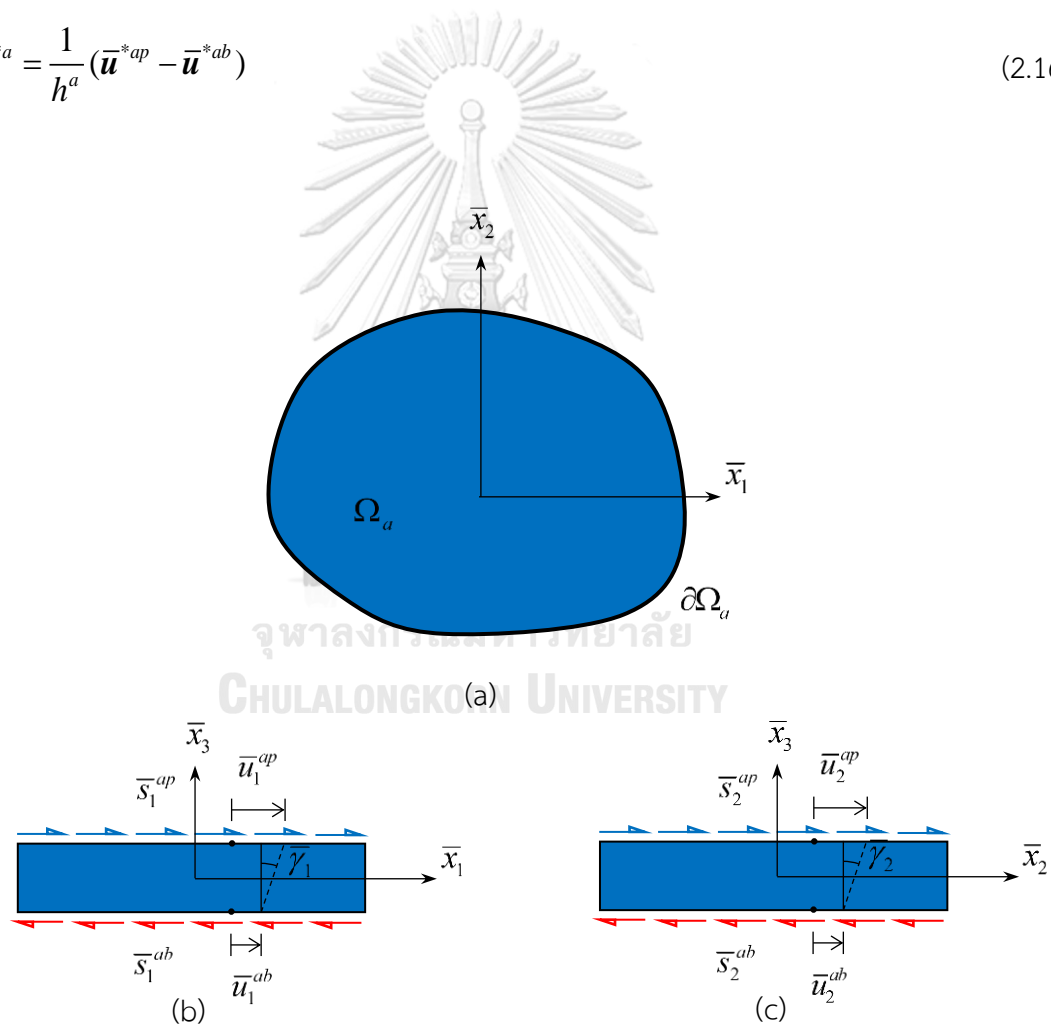


Figure 2.4 Schematic of (a) a generic adhesive layer in local coordinate system, (b) adhesive layer under the action in \bar{x}_1 direction, and (c) adhesive layer under the action in \bar{x}_2 direction.

where $\bar{\mathbf{u}}^{*ap}$ and $\bar{\mathbf{u}}^{*ab}$ are values of $\bar{\mathbf{u}}^{*a}$ at the interface connecting to the patch and the cracked body, respectively. The out-of-plane shear stress $\bar{\boldsymbol{\sigma}}^{*a} = \{\bar{\sigma}_{31}^a \ \bar{\sigma}_{32}^a\}^T$ induced within the layer can be readily obtained from the constitutive relation

$$\bar{\boldsymbol{\sigma}}^{*a} = G^a \bar{\boldsymbol{\varepsilon}}^{*a} \quad (2.17)$$

where G^a denotes the elastic shear modulus of the adhesive material. To ensure the equilibrium of the adhesive layer, the unknown shear tractions \mathbf{s}^{ap} and \mathbf{s}^{ab} must satisfy the relation

$$\bar{\mathbf{s}}^{*ap} = -\bar{\mathbf{s}}^{*ab} = \bar{\boldsymbol{\sigma}}^{*a} \quad (2.18)$$

where $\bar{\mathbf{s}}^{*ap} = \{\bar{s}_1^{ap} \ \bar{s}_2^{ap}\}$ and $\bar{\mathbf{s}}^{*ab} = \{\bar{s}_1^{ab} \ \bar{s}_2^{ab}\}$ contain local components of \mathbf{s}^{ap} and \mathbf{s}^{ab} , respectively. Combining (2.16) and (2.17) yields

$$\bar{\boldsymbol{\sigma}}^{*a} = \frac{G^a}{h^a} (\bar{\mathbf{u}}^{*ap} - \bar{\mathbf{u}}^{*ab}) \quad (2.19)$$

The alternative weak-statement of (2.19) can be established using the weighted residual technique to obtain

$$\int_{\Omega_a} \frac{h^a}{G^a} (\bar{\mathbf{w}}^a)^T \bar{\boldsymbol{\sigma}}^{*a} dA = \int_{\Omega_a} (\bar{\mathbf{w}}^a)^T \bar{\mathbf{u}}^{*ap} dA - \int_{\Omega_a} (\bar{\mathbf{w}}^a)^T \bar{\mathbf{u}}^{*ab} dA \quad (2.20)$$

where $\bar{\mathbf{w}}^a$ is any sufficiently smooth test function. The weak-form equation (2.20) and the equilibrium conditions (2.18) form the governing equations for each adhesive layer.

2.5 GOVERNING EQUATIONS FOR CRACKED BODY

The response of the cracked body resulting from the domain decomposition, as illustrated in Figure 2.2(c), is modeled by a classical theory of three-dimensional linear elasticity. The key governing equations can be readily established based on the boundary integral formulation following the development of Rungamornrat and Mear (2008).

A pair of boundary integral equations for the displacement and the traction for a body containing cracks as shown in Figure 2.2(c) is given by

$$\begin{aligned} \frac{1}{2} \int_{S_0} \tilde{\tau}_p(\mathbf{y}) u_p^b(\mathbf{y}) dS(\mathbf{y}) &= \int_{S_0} \tilde{\tau}_p(\mathbf{y}) \int_{S_0} U_j^p(\boldsymbol{\xi} - \mathbf{y}) t_j^b(\boldsymbol{\xi}) dS(\boldsymbol{\xi}) dS(\mathbf{y}) \\ &+ \int_{S_0} \tilde{\tau}_p(\mathbf{y}) \int_S G_{mj}^p(\boldsymbol{\xi} - \mathbf{y}) D_m v_j^b(\boldsymbol{\xi}) dS(\boldsymbol{\xi}) dS(\mathbf{y}) \\ &- \int_{S_0} \tilde{\tau}_p(\mathbf{y}) \int_S n_i(\boldsymbol{\xi}) H_{ij}^p(\boldsymbol{\xi} - \mathbf{y}) v_j^b(\boldsymbol{\xi}) dS(\boldsymbol{\xi}) dS(\mathbf{y}) \end{aligned} \quad (2.21)$$

$$\begin{aligned} -\frac{1}{2} \int_S \tilde{u}_k(\mathbf{y}) \tau_k^b(\mathbf{y}) dS(\mathbf{y}) &= \int_S D_l \tilde{u}_k(\mathbf{y}) \int_S C_{mj}^{lk}(\boldsymbol{\xi} - \mathbf{y}) D_m v_j^b(\boldsymbol{\xi}) dS(\boldsymbol{\xi}) dS(\mathbf{y}) \\ &+ \int_S D_l \tilde{u}_k(\mathbf{y}) \int_{S_0} G_{jk}^l(\boldsymbol{\xi} - \mathbf{y}) t_j^b(\boldsymbol{\xi}) dS(\boldsymbol{\xi}) dS(\mathbf{y}) \\ &+ \int_S \tilde{u}_k(\mathbf{y}) \int_{S_0} n_l(\mathbf{y}) H_{lk}^j(\boldsymbol{\xi} - \mathbf{y}) t_j^b(\boldsymbol{\xi}) dS(\boldsymbol{\xi}) dS(\mathbf{y}) \end{aligned} \quad (2.22)$$

where $S \equiv S_0 \cup S_c^+$ denotes the whole boundary of the damaged domain; $\tilde{\tau}_p$ is any sufficiently smooth test function defined on the ordinary boundary S_0 ; \tilde{u}_k is any sufficiently smooth test function defined on the total boundary S ; u_p^b and t_j^b are components of the displacement and traction on the ordinary boundary S_0 of the cracked body; n_i are components of the outward unit normal vector to the total boundary S ; $D_m = n_i \varepsilon_{ism} \partial / \partial \xi_s$ or $D_m = n_i \varepsilon_{ism} \partial / \partial y_s$ denotes the surface differential operator; U_j^p , C_{mj}^{lk} , G_{mj}^p , and H_{ij}^p are known fundamental solutions; and v_j^b and τ_k^b are data defined by

$$v_j^b(\boldsymbol{\xi}) = \begin{cases} u_j^b(\boldsymbol{\xi}), & \boldsymbol{\xi} \in S_0 \\ \Delta u_j^b(\boldsymbol{\xi}), & \boldsymbol{\xi} \in S_c^+ \end{cases} \quad (2.23)$$

$$\tau_k^b(\boldsymbol{\xi}) = \begin{cases} t_k^b(\boldsymbol{\xi}), & \boldsymbol{\xi} \in S_0 \\ \Delta t_k^b(\boldsymbol{\xi}), & \boldsymbol{\xi} \in S_c^+ \end{cases} \quad (2.24)$$

In which $\Delta u_j^b(\boldsymbol{\xi}) = u_j^+ - u_j^-$ denotes the relative crack-face displacement and $\Delta t_k^b(\boldsymbol{\xi}) = t_k^{0+} - t_k^{0-}$ denotes the jump in the crack-face traction. In particular, for the self-equilibrated crack-face traction, it yields $\Delta t_k^b(\boldsymbol{\xi}) = 2t_k^{0+}$. For general anisotropy, all involved fundamental solutions U_j^p , C_{mj}^{lk} , G_{mj}^p , and H_{ij}^p were obtained explicitly by Rungamornrat and Mear (2008) as

$$U_j^p(\boldsymbol{\xi} - \mathbf{y}) = \frac{1}{8\pi^2 r} \oint_{z \cdot \mathbf{r} = 0} (\mathbf{z}, \mathbf{z})_{jp}^{-1} ds(\mathbf{z}) \quad (2.25)$$

$$G_{mj}^p(\boldsymbol{\xi} - \mathbf{y}) = \varepsilon_{abm} E_{ajdc} \frac{1}{8\pi^2 r} \oint_{z \cdot \mathbf{r} = 0} z_b z_c (\mathbf{z}, \mathbf{z})_{dp}^{-1} ds(\mathbf{z}) \quad (2.26)$$

$$C_{mj}^{tk}(\boldsymbol{\xi} - \mathbf{y}) = \varepsilon_{pam} \varepsilon_{pbt} (E_{bknd} E_{ajeo} - \frac{1}{3} E_{ajkb} E_{dneo}) \frac{1}{8\pi^2 r} \oint_{z \cdot \mathbf{r} = 0} z_o z_d (\mathbf{z}, \mathbf{z})_{en}^{-1} ds(\mathbf{z}) \quad (2.27)$$

$$H_{ij}^p(\boldsymbol{\xi} - \mathbf{y}) = -\frac{1}{4\pi r^3} (\xi_i - y_i) \delta_{jp} \quad (2.28)$$

where $\mathbf{r} = \boldsymbol{\xi} - \mathbf{y}$, $r = |\mathbf{r}|$, \mathbf{z} is a unit vector on the plane normal to \mathbf{r} , E_{mijpn} denotes the elastic moduli of the material constituting the cracked body, $(\mathbf{z}, \mathbf{z})_{jp} = z_m E_{mijpn} z_n$, $(\mathbf{z}, \mathbf{z})^{-1}$ is the inverse of the matrix (\mathbf{z}, \mathbf{z}) , and δ_{ij} , ε_{ijk} are standard Kronecker and alternating symbols, respectively. It is worth noting that besides its vast capability to treat cracked bodies of general configurations, material anisotropy, and general loading conditions, the pair of boundary integral equations (2.21) and (2.22) are constructed in a weak-form well-suited for use as the basis of finite element and boundary element coupling procedure. In addition, all involved integrals contain only weakly singular kernels allowing the interpretation of singular integrals in the sense of Riemann sum and rendering the use of continuous interpolation functions in the approximation of unknown data.

To establish a set of integral equations governing the cracked body shown in Figure 2.2(c), the pair of weak-form integral equations is applied properly to each portion of the ordinary boundary and the crack surface as follows. On the surface S_u on which the displacement is fully known, the displacement integral equation (2.21) is employed by restricting the choice of test functions $\tilde{\tau}_p$ such that they vanish on the surface $S_t \cup S_a$ whereas on the surface S_t and the crack surface S_c^+ on which the tractions are prescribed, the traction integral equation (2.22) is utilized by choosing the test functions \tilde{u}_k such that they vanish identically on the surface $S_u \cup S_a \cup S_c^+$ and the surface S_0 , respectively. On the surface S_a connecting to the adhesive layer, both the shear tractions and the displacements are unknown a priori and the traction integral equation (2.22) is applied with the test functions satisfying

the condition $\tilde{\mathbf{u}}_k = \mathbf{0}$ on $S_u \cup S_t \cup S_c^+$. Following such the procedure, there results in a system of four weak-form boundary integral equations:

$$\mathcal{A}_{uu}(\tilde{\boldsymbol{\tau}}, \mathbf{t}^{bu}) + \mathcal{B}_{ut}(\tilde{\boldsymbol{\tau}}, \mathbf{u}^{bt}) + \mathcal{B}_{uc}(\tilde{\boldsymbol{\tau}}, \Delta \mathbf{u}^b) + \mathcal{B}_{ua}(\tilde{\boldsymbol{\tau}}, \mathbf{u}^{ba}) + \mathcal{A}_{ua}(\tilde{\boldsymbol{\tau}}, \mathbf{s}^{ba}) = \mathcal{R}_u(\tilde{\boldsymbol{\tau}}) \quad (2.29)$$

$$\mathcal{B}_{ut}(\mathbf{t}^{bu}, \tilde{\mathbf{u}}) + \mathcal{C}_{it}(\tilde{\mathbf{u}}, \mathbf{u}^{bt}) + \mathcal{C}_{ic}(\tilde{\mathbf{u}}, \Delta \mathbf{u}^b) + \mathcal{C}_{ia}(\tilde{\mathbf{u}}, \mathbf{u}^{ba}) + \mathcal{B}_{at}(\mathbf{s}^{ba}, \tilde{\mathbf{u}}) = \mathcal{R}_t(\tilde{\mathbf{u}}) \quad (2.30)$$

$$\mathcal{B}_{uc}(\mathbf{t}^{bu}, \tilde{\mathbf{u}}) + \mathcal{C}_{ct}(\tilde{\mathbf{u}}, \mathbf{u}^{bt}) + \mathcal{C}_{cc}(\tilde{\mathbf{u}}, \Delta \mathbf{u}^b) + \mathcal{C}_{ca}(\tilde{\mathbf{u}}, \mathbf{u}^{ba}) + \mathcal{B}_{ac}(\mathbf{s}^{ba}, \tilde{\mathbf{u}}) = \mathcal{R}_c(\tilde{\mathbf{u}}) \quad (2.31)$$

$$\mathcal{B}_{ua}(\mathbf{t}^{bu}, \tilde{\mathbf{u}}) + \mathcal{C}_{ut}(\tilde{\mathbf{u}}, \mathbf{u}^{bt}) + \mathcal{C}_{ac}(\tilde{\mathbf{u}}, \Delta \mathbf{u}^b) + \mathcal{C}_{aa}(\tilde{\mathbf{u}}, \mathbf{u}^{ba}) + \mathcal{B}_{aa}(\mathbf{s}^{ba}, \tilde{\mathbf{u}}) + \mathcal{D}_a(\tilde{\mathbf{u}}, \mathbf{s}^{ba}) = \mathcal{R}_a(\tilde{\mathbf{u}}) \quad (2.32)$$

where the linear integral operators $\mathcal{A}_{PQ}, \mathcal{B}_{PQ}, \mathcal{C}_{PQ}, \mathcal{D}_P$ with $P, Q \in \{u, t, c, a\}$ are defined by

$$\mathcal{A}_{pQ}(\mathbf{X}, \mathbf{Y}) = \int_{S_p} X_p(\mathbf{y}) \int_{S_Q} U_j^p(\boldsymbol{\xi} - \mathbf{y}) Y_j(\boldsymbol{\xi}) dS(\boldsymbol{\xi}) dS(\mathbf{y}) \quad (2.33)$$

$$\begin{aligned} \mathcal{B}_{pQ}(\mathbf{X}, \mathbf{Y}) &= \int_{S_p} X_p(\mathbf{y}) \int_{S_Q} G_{mj}^p(\boldsymbol{\xi} - \mathbf{y}) D_m Y_j(\boldsymbol{\xi}) dS(\boldsymbol{\xi}) dS(\mathbf{y}) \\ &\quad - \int_{S_p} X_p(\mathbf{y}) \int_{S_Q} n_i(\boldsymbol{\xi}) H_{ij}^p(\boldsymbol{\xi} - \mathbf{y}) Y_j(\boldsymbol{\xi}) dS(\boldsymbol{\xi}) dS(\mathbf{y}) \end{aligned} \quad (2.34)$$

$$\mathcal{C}_{pQ}(\mathbf{X}, \mathbf{Y}) = \int_{S_p} D_i X_k(\mathbf{y}) \int_{S_Q} C_{mj}^{tk}(\boldsymbol{\xi} - \mathbf{y}) D_m Y_j(\boldsymbol{\xi}) dS(\boldsymbol{\xi}) dS(\mathbf{y}) \quad (2.35)$$

$$\mathcal{D}_p(\mathbf{X}, \mathbf{Y}) = \frac{1}{2} \int_{S_p} X_i(\mathbf{y}) Y_i(\mathbf{y}) dS(\mathbf{y}) \quad (2.36)$$

in which \mathbf{X}, \mathbf{Y} are vector value functions. The linear integral operators $\mathcal{R}_u, \mathcal{R}_t, \mathcal{R}_c$ and \mathcal{R}_a on the right hand side of (2.29) - (2.32) involve prescribed data defined by

$$\mathcal{R}_u(\tilde{\boldsymbol{\tau}}) = \mathcal{D}_u(\tilde{\boldsymbol{\tau}}, \mathbf{u}^{bu}) - \mathcal{A}_{ua}(\tilde{\boldsymbol{\tau}}, \mathbf{q}^{ba}) - \mathcal{A}_{ut}(\tilde{\boldsymbol{\tau}}, \mathbf{t}^{bt}) - \mathcal{B}_{uu}(\tilde{\boldsymbol{\tau}}, \mathbf{u}^{bu}) \quad (2.37)$$

$$\mathcal{R}_t(\tilde{\mathbf{u}}) = -\mathcal{D}_t(\tilde{\mathbf{u}}, \mathbf{t}^{bt}) - \mathcal{B}_{it}(\mathbf{t}^{bt}, \tilde{\mathbf{u}}) - \mathcal{B}_{at}(\mathbf{q}^{ba}, \tilde{\mathbf{u}}) - \mathcal{C}_{iu}(\tilde{\mathbf{u}}, \mathbf{u}^{bu}) \quad (2.38)$$

$$\mathcal{R}_c(\tilde{\mathbf{u}}) = -\mathcal{D}_c(\tilde{\mathbf{u}}, \Delta \mathbf{u}^b) - \mathcal{B}_{ic}(\mathbf{t}^{bt}, \tilde{\mathbf{u}}) - \mathcal{B}_{ac}(\mathbf{q}^{ba}, \tilde{\mathbf{u}}) - \mathcal{C}_{cu}(\tilde{\mathbf{u}}, \mathbf{u}^{bu}) \quad (2.39)$$

$$\mathcal{R}_a(\tilde{\mathbf{u}}) = -\mathcal{D}_a(\tilde{\mathbf{u}}, \mathbf{q}^{ba}) - \mathcal{B}_{ia}(\mathbf{t}^{bt}, \tilde{\mathbf{u}}) - \mathcal{B}_{aa}(\mathbf{q}^{ba}, \tilde{\mathbf{u}}) - \mathcal{C}_{au}(\tilde{\mathbf{u}}, \mathbf{u}^{bu}) \quad (2.40)$$

It is remarked that the system of integral equations (2.29) - (2.32) contains five unknown functions including the unknown traction \mathbf{t}^{bu} on the surface S_u , the unknown displacement \mathbf{u}^{bt} on the surface S_t , the unknown relative crack-face

displacement $\Delta \mathbf{u}^b$, and the unknown displacement \mathbf{u}^{ba} and the unknown shear traction \mathbf{s}^{ba} on the surface S_a .

2.6 GOVERNING EQUATIONS FOR ENTIRE SYSTEM

The continuity conditions of the total displacements at the interface (2.3) and (2.6) also imply the continuity of the in-plane displacements, i.e.,

$$\bar{\mathbf{u}}^{*p} = \bar{\mathbf{u}}^{*ap} \quad (2.41)$$

$$\bar{\mathbf{u}}^{*ba} = \bar{\mathbf{u}}^{*ab} \quad (2.42)$$

where $\bar{\mathbf{u}}^{*ba}$ is a vector containing only local in-plane components of the global total displacement \mathbf{u}^{ba} on the surface S_a of the cracked body. From the law of coordinate transformation, $\bar{\mathbf{u}}^{*ba}$ can be related to \mathbf{u}^{ba} by

$$\bar{\mathbf{u}}^{*ba} = \mathbf{a} \mathbf{T} \mathbf{u}^{ba} \quad (2.43)$$

where \mathbf{T} is a standard transformation matrix relating the bases of the global and local coordinate systems and \mathbf{a} is the selection matrix defined by

$$\mathbf{a} = \begin{bmatrix} 1 & 0 & 0 \\ 0 & 1 & 0 \end{bmatrix} \quad (2.44)$$

Similarly, the global continuity conditions (2.4) and (2.7) of the shear tractions on the two interfaces also imply

$$\bar{\mathbf{s}}^{*pa} + \bar{\mathbf{s}}^{*ap} = \mathbf{0} \quad (2.45)$$

$$\bar{\mathbf{s}}^{*ba} + \bar{\mathbf{s}}^{*ab} = \mathbf{0} \quad (2.46)$$

where $\bar{\mathbf{s}}^{*ba}$ is a vector containing only local components of the global shear traction \mathbf{s}^{ba} exerted to the surface S_a by the adhesive layer. Similarly, \mathbf{s}^{ba} can be related to $\bar{\mathbf{s}}^{*ba}$ by

$$\mathbf{s}^{ba} = \mathbf{T}^T \mathbf{a}^T \bar{\mathbf{s}}^{*ba} \quad (2.47)$$

Combining (2.45) - (2.47) and the relation (2.18) leads to

$$\bar{s}^{*pa} = -\bar{\sigma}^{*a} \quad (2.48)$$

$$\mathbf{s}^{ba} = \mathbf{T}^T \mathbf{a}^T \bar{\sigma}^{*a} \quad (2.49)$$

The governing equations for the repaired cracked body shown in Figure 2.1 can now be obtained by combining that for the patch (2.15), that for the adhesive layer (2.20) and those for the cracked body (2.29)-(2.32) together with the conditions (2.41)-(2.43), (2.48)-(2.49) and the fact that the surface S_a and the two-dimensional domains Ω_p and Ω_a are identical. The final system can be rewritten as

$$\int_{S_a} h_p (\mathbf{L}\bar{\mathbf{w}}^p)^T \mathbf{C}^{*p} \mathbf{L}\bar{\mathbf{u}}^{*p} dA + \int_{S_a} (\bar{\mathbf{w}}^p)^T \bar{\sigma}^{*a} dA = \int_{S_a} (\bar{\mathbf{w}}^p)^T \bar{s}^{*p0} dA \quad (2.50)$$

$$\int_{S_a} \frac{h^a}{G^a} (\bar{\mathbf{w}}^a)^T \bar{\sigma}^{*a} dA = \int_{S_a} (\bar{\mathbf{w}}^a)^T \bar{\mathbf{u}}^{*p} dA - \int_{S_a} (\bar{\mathbf{w}}^a)^T \mathbf{a}^T \mathbf{u}^{ba} dA \quad (2.51)$$

$$\mathcal{A}_{uu}(\tilde{\mathbf{r}}, \mathbf{t}^{bu}) + \mathcal{B}_{ut}(\tilde{\mathbf{r}}, \mathbf{u}^{bt}) + \mathcal{B}_{uc}(\tilde{\mathbf{r}}, \Delta \mathbf{u}^b) + \mathcal{B}_{ua}(\tilde{\mathbf{r}}, \mathbf{u}^{ba}) + \mathcal{A}_{ua}(\tilde{\mathbf{r}}, \mathbf{T}^T \mathbf{a}^T \bar{\sigma}^{*a}) = \mathcal{R}_t(\tilde{\mathbf{r}}) \quad (2.52)$$

$$\mathcal{B}_{ut}(\mathbf{t}^{bu}, \tilde{\mathbf{u}}) + \mathcal{C}_{tt}(\tilde{\mathbf{u}}, \mathbf{u}^{bt}) + \mathcal{C}_{tc}(\tilde{\mathbf{u}}, \Delta \mathbf{u}^b) + \mathcal{C}_{ta}(\tilde{\mathbf{u}}, \mathbf{u}^{ba}) + \mathcal{B}_{at}(\mathbf{T}^T \mathbf{a}^T \bar{\sigma}^{*a}, \tilde{\mathbf{u}}) = \mathcal{R}_t(\tilde{\mathbf{u}}) \quad (2.53)$$

$$\mathcal{B}_{uc}(\mathbf{t}^{bu}, \tilde{\mathbf{u}}) + \mathcal{C}_{ct}(\tilde{\mathbf{u}}, \mathbf{u}^{bt}) + \mathcal{C}_{cc}(\tilde{\mathbf{u}}, \Delta \mathbf{u}^b) + \mathcal{C}_{ca}(\tilde{\mathbf{u}}, \mathbf{u}^{ba}) + \mathcal{B}_{ac}(\mathbf{T}^T \mathbf{a}^T \bar{\sigma}^{*a}, \tilde{\mathbf{u}}) = \mathcal{R}_c(\tilde{\mathbf{u}}) \quad (2.54)$$

$$\mathcal{B}_{ua}(\mathbf{t}^{bu}, \tilde{\mathbf{u}}) + \mathcal{C}_{at}(\tilde{\mathbf{u}}, \mathbf{u}^{bt}) + \mathcal{C}_{ac}(\tilde{\mathbf{u}}, \Delta \mathbf{u}^b) + \mathcal{C}_{aa}(\tilde{\mathbf{u}}, \mathbf{u}^{ba}) + \mathcal{B}_{aa}(\mathbf{T}^T \mathbf{a}^T \bar{\sigma}^{*a}, \tilde{\mathbf{u}}) + \mathcal{D}_a(\tilde{\mathbf{u}}, \mathbf{T}^T \mathbf{a}^T \bar{\sigma}^{*a}) = \mathcal{R}_a(\tilde{\mathbf{u}}) \quad (2.55)$$

It is seen that the system of equations (2.50)-(2.55) forms a sufficient set of conditions for determining the six unknown functions \mathbf{t}^{bu} , \mathbf{u}^{bt} , $\Delta \mathbf{u}^b$, \mathbf{u}^{ba} , $\bar{\sigma}^{*a}$, and $\bar{\mathbf{u}}^{*p}$.

CHAPTER 3

SOLUTION PROCEDURE

This chapter summarizes the computational procedure for determining numerical solutions of a system of governing equations (2.50)-(2.55). A finite element technique is adopted to handle the weak-form equations governing the patches and the adhesive layers whereas the weakly singular boundary integral equation method is applied to discretize the governing integral equations for the cracked body. A post-process routine for calculating the stress intensity factors along the crack front is also outlined at the end of this chapter.



3.1 SOLUTION DISCRETIZATION

To discretize the governing equations for the patches and the adhesive layers (2.50) and (2.51), a conventional finite element procedure for two-dimensional problems (e.g., Bathe, 2006; Hughes, 2012; Zienkiewicz et al., 2000) is adopted. The unknown shear stress within the adhesive layer $\bar{\sigma}^{*a}$, the unknown displacement of the patch \bar{u}^{*p} , the unknown displacement u^{ba} on the repaired surface S_a of the cracked body and all involved test functions (i.e., \bar{w}^p and \bar{w}^a) are approximated by standard basis functions constructed locally on a finite element mesh consisting of standard, two-dimensional, isoparametric, C^0 -elements. The approximations are given explicitly by

$$\bar{u}^{*p} = \sum_{i=1}^{N_p} \Phi_{(i)}^p \mathbf{U}_{(i)}^p = \mathbf{\Phi}^p \mathbf{U}^p \quad (3.1)$$

$$\bar{\sigma}^{*a} = \sum_{i=1}^{N_a} \Phi_{(i)}^a \Sigma_{(i)}^a = \mathbf{\Phi}^a \Sigma^a \quad (3.2)$$

$$u^{ba} = \sum_{i=1}^{N_{ba}} \Phi_{(i)}^{ba} \mathbf{U}_{(i)}^{ba} = \mathbf{\Phi}^{ba} \mathbf{U}^{ba} \quad (3.3)$$

$$\bar{w}^p = \sum_{i=1}^{N_p} \Phi_{(i)}^p \mathbf{W}_{(i)}^p = \mathbf{\Phi}^p \mathbf{W}^p \quad (3.4)$$

$$\bar{w}^a = \sum_{i=1}^{N_a} \Phi_{(i)}^a \mathbf{W}_{(i)}^a = \mathbf{\Phi}^a \mathbf{W}^a \quad (3.5)$$

where N_p , N_a and N_{ba} denote the number of nodes in the finite element mesh of the patch, adhesive layer, and the surface S_a , respectively; $\Phi_{(i)}^p$, $\Phi_{(i)}^a$ and $\Phi_{(i)}^{ba}$ are nodal basic functions associated with the i^{th} node of the patch, the adhesive layer, and the surface S_a , respectively; $\mathbf{U}_{(i)}^p$, $\Sigma_{(i)}^a$ and $\mathbf{U}_{(i)}^{ba}$ are the displacement of the patch, the shear stress within the adhesive layer, and the displacement of the surface S_a at the i^{th} node, respectively; $\mathbf{W}_{(i)}^p$ and $\mathbf{W}_{(i)}^a$ are the arbitrary vectors at the i^{th} node of the patch and the adhesive layer, respectively; \mathbf{U}^p , Σ^a and \mathbf{U}^{ba} are vectors containing all the nodal displacements $\mathbf{U}_{(i)}^p$, the nodal shear stress $\Sigma_{(i)}^a$ and the nodal displacements $\mathbf{U}_{(i)}^{ba}$, respectively; \mathbf{W}^p and \mathbf{W}^a are vectors containing all the arbitrary vectors $\mathbf{W}_{(i)}^p$ and $\mathbf{W}_{(i)}^a$, respectively; and Φ^p , Φ^a and Φ^{ba} are the corresponding matrix storing the nodal basis functions $\Phi_{(i)}^p$, $\Phi_{(i)}^a$ and $\Phi_{(i)}^{ba}$, respectively. In the present study, finite element meshes used for constructing the basis functions $\Phi_{(i)}^p$ for the patch, $\Phi_{(i)}^a$ for the adhesive layer and $\Phi_{(i)}^{ba}$ for the surface S_a are taken to be conforming. This implies that the continuity of the displacements and traction along the interface can be enforced in a strong sense. Note in addition that nodes located along the surface breaking line on the surface S_a (a line where the surface breaking crack intersects the surface S_a) excluding the vertices (points where the crack front intersects the surface S_a) must be treated as the double nodes; i.e., they contain twice the number of degree of freedom of that of the regular nodes. Similarly, nodes along the surface breaking line of the adhesive layer must be also treated as the double nodes; i.e., each of those nodes contains 4 shear-stress degrees of freedom instead of 2 degrees of freedom as for the regular nodes.

To discretize the weak-form boundary integral equations governing the cracked body (2.52)-(2.55), Galerkin-based procedure the same as that utilized by Rungamornrat and Mear (2008) is adopted. Due to the weakly singular nature of all involved integrals, all unknown functions and test functions can be discretized using continuous basis functions constructed locally on a finite element mesh over portions of the ordinary boundary S_0 and the crack surface S_c^+ . Specifically, the unknown traction \mathbf{t}^{bu} and the test function $\tilde{\boldsymbol{\tau}}$ on the surfaces S_u , the unknown displacement \mathbf{u}^{bt} and the test function $\tilde{\mathbf{u}}$ on the surface S_t , and the unknown

relative crack-face displacement $\Delta \mathbf{u}^b$ and the test function $\tilde{\mathbf{u}}$ on the crack surface S_c^+ are approximated by

$$\mathbf{t}^{bu} = \sum_{i=1}^{N_{bu}} \Phi_{(i)}^{bu} \mathbf{T}_{(i)}^{bu} = \mathbf{\Phi}^{bu} \mathbf{T}^{bu}; \quad \tilde{\boldsymbol{\tau}} = \sum_{i=1}^{N_{bu}} \Phi_{(i)}^{bu} \tilde{\mathbf{T}}_{(i)}^{bu} = \mathbf{\Phi}^{bu} \tilde{\mathbf{T}}^{bu} \quad (3.6)$$

$$\mathbf{u}^{bt} = \sum_{i=1}^{N_{bt}} \Phi_{(i)}^{bt} \mathbf{U}_{(i)}^{bt} = \mathbf{\Phi}^{bt} \mathbf{U}^{bt}; \quad \tilde{\mathbf{u}} = \sum_{i=1}^{N_{bt}} \Phi_{(i)}^{bt} \tilde{\mathbf{U}}_{(i)}^{bt} = \mathbf{\Phi}^{bt} \tilde{\mathbf{U}}^{bt} \quad (3.7)$$

$$\Delta \mathbf{u}^b = \sum_{i=1}^{N_{bc}} \Phi_{(i)}^{bc} \Delta \mathbf{U}_{(i)}^{bc} = \mathbf{\Phi}^{bc} \Delta \mathbf{U}^{bc}; \quad \tilde{\mathbf{u}} = \sum_{i=1}^{N_{bc}} \Phi_{(i)}^{bc} \tilde{\mathbf{U}}_{(i)}^{bc} = \mathbf{\Phi}^{bc} \tilde{\mathbf{U}}^{bc} \quad (3.8)$$

where N_{bu} , N_{bt} and N_{bc} are the number of nodes used in the discretization of quantities on the surfaces S_u , S_t and S_c^+ , respectively; $\{\Phi_{(i)}^{bu}, \mathbf{T}_{(i)}^{bu}, \tilde{\mathbf{T}}_{(i)}^{bu}\}$, $\{\Phi_{(i)}^{bt}, \mathbf{U}_{(i)}^{bt}, \tilde{\mathbf{U}}_{(i)}^{bt}\}$ and $\{\Phi_{(i)}^{bc}, \Delta \mathbf{U}_{(i)}^{bc}, \tilde{\mathbf{U}}_{(i)}^{bc}\}$ are the nodal basic functions, the nodal unknowns and the nodal arbitrary vectors associated with the i^{th} node on the surface S_u , S_t and S_c^+ , respectively; $\{\mathbf{T}^{bu}, \tilde{\mathbf{T}}^{bu}\}$, $\{\mathbf{U}^{bt}, \tilde{\mathbf{U}}^{bt}\}$ and $\{\mathbf{U}^{bc}, \tilde{\mathbf{U}}^{bc}\}$ are vectors containing all the nodal unknowns and nodal arbitrary vectors on the surface S_u , S_t and S_c^+ , respectively; and $\mathbf{\Phi}^{bu}$, $\mathbf{\Phi}^{bt}$ and $\mathbf{\Phi}^{bc}$ are the corresponding matrix storing the nodal basis functions $\Phi_{(i)}^{bu}$, $\Phi_{(i)}^{bt}$ and $\Phi_{(i)}^{bc}$, respectively. On the repaired surface S_a , the unknown displacement \mathbf{u}^{ba} is approximated by (3.3) whereas the approximation of the unknown shear traction \mathbf{s}^{ba} is achieved by (3.2) and the relationship (2.49). It is also important to remark that due to the regularity of solutions on the ordinary boundary, standard, two-dimensional, isoparametric, C^0 -elements are employed in the discretization. On the crack surface, it is known that the relative crack-face displacement possess an unbounded gradient at the crack front and this must be properly treated in the approximation. In the present study, special crack-tip elements proposed by Rungamornrat and Mear (2008) are employed to enhance the near-front approximation. With the use of these special elements, it has been found that relatively coarse meshes can be employed to accurately capture the crack-face data.

3.2 DISCRETIZED FORM OF GOVERNING EQUATIONS

By substituting the approximations (3.1), (3.2) and (3.4) into the weak-form equation (2.50) for the patches together with using the arbitrariness of \mathbf{W}^p , it gives rise to

$$\mathbf{C}_1 \boldsymbol{\Sigma}^a + \mathbf{C}_2 \mathbf{U}^p = \mathbf{R}_1 \quad (3.9)$$

where the coefficient matrices \mathbf{C}_1 and \mathbf{C}_2 and the load vector \mathbf{R}_1 are defined by

$$\mathbf{C}_1 = \int_{S_a} (\boldsymbol{\Phi}^p)^T \boldsymbol{\Phi}^a dA \quad (3.10)$$

$$\mathbf{C}_2 = \int_{S_a} h_p (\mathbf{L} \boldsymbol{\Phi}^p)^T \mathbf{C}^{*p} \mathbf{L} \boldsymbol{\Phi}^p dA \quad (3.11)$$

$$\mathbf{R}_1 = \int_{S_a} (\boldsymbol{\Phi}^p)^T \bar{s}^{*p0} dA \quad (3.12)$$

The coefficient matrices \mathbf{C}_1 and \mathbf{C}_2 and the load vector \mathbf{R}_1 can be readily constructed using a standard assembly procedure together with Gaussian quadrature to evaluate all regular integrals over elements resulting from the discretization.

Similarly, by applying the approximations (3.1)-(3.3) and (3.5) to the weak-form equation (2.51) for the adhesive layers, it leads to a system of linear algebraic equations:

$$\mathbf{C}_3 \mathbf{U}^{ba} + \mathbf{C}_4 \boldsymbol{\Sigma}^a + \mathbf{C}_5 \mathbf{U}^p = \mathbf{R}_2 \quad (3.13)$$

where the coefficient matrices \mathbf{C}_3 , \mathbf{C}_4 and \mathbf{C}_5 and the load vector \mathbf{R}_2 are given by

$$\mathbf{C}_3 = \int_{S_a} (\boldsymbol{\Phi}^a)^T \mathbf{a} \mathbf{T} \boldsymbol{\Phi}^{ba} dA \quad (3.14)$$

$$\mathbf{C}_4 = \int_{S_a} \frac{h^a}{G^a} (\boldsymbol{\Phi}^a)^T \boldsymbol{\Phi}^a dA \quad (3.15)$$

$$\mathbf{C}_5 = - \int_{S_a} (\boldsymbol{\Phi}^a)^T \boldsymbol{\Phi}^p dA \quad (3.16)$$

$$\mathbf{R}_2 = \mathbf{0} \quad (3.17)$$

Again, the standard assembly procedure is adopted, together with the numerical integration by Gaussian quadrature, to construct the three coefficient matrices \mathbf{C}_3 , \mathbf{C}_4 and \mathbf{C}_5 .

Finally, a set of governing boundary integral equations (2.52)-(2.55) for the cracked body can be discretized, with the use of (3.2)-(3.3) and (3.6)-(3.8), into a system of linear algebraic equations

$$\begin{bmatrix} \mathbf{A}_{uu} & \mathbf{B}_{ut} & \mathbf{B}_{uc} & \mathbf{B}_{ua} & \mathbf{A}_{ua} \\ \mathbf{B}_{ut}^T & \mathbf{C}_{tt} & \mathbf{C}_{tc} & \mathbf{C}_{ta} & \mathbf{B}_{at}^T \\ \mathbf{B}_{uc}^T & \mathbf{C}_{tc}^T & \mathbf{C}_{cc} & \mathbf{C}_{ca} & \mathbf{B}_{ac}^T \\ \mathbf{B}_{ua}^T & \mathbf{C}_{ta}^T & \mathbf{C}_{ca}^T & \mathbf{C}_{aa} & \mathbf{B}_{aa}^T + \mathbf{D}_a \end{bmatrix} \begin{Bmatrix} \mathbf{T}^{bu} \\ \mathbf{U}^{bt} \\ \Delta \mathbf{U}^{bc} \\ \mathbf{U}^{ba} \\ \Sigma^a \end{Bmatrix} = \begin{Bmatrix} \mathbf{R}_3 \\ \mathbf{R}_4 \\ \mathbf{R}_5 \\ \mathbf{R}_6 \end{Bmatrix} \quad (3.18)$$

where entries of coefficient matrices \mathbf{A}_{PQ} , \mathbf{B}_{PQ} , \mathbf{C}_{PQ} for $P, Q \in \{u, t, a, c\}$ and \mathbf{D}_a are defined explicitly by

$$[\mathbf{A}_{PQ}]_{3(i-1)+k, 3(j-1)+l} = \int_{S_p} \Phi_{(i)}^{bP}(\mathbf{y}) \int_{S_q} U_l^k(\xi - \mathbf{y}) \Phi_{(j)}^{bQ}(\xi) dS(\xi) dS(\mathbf{y}) \quad (3.19)$$

$$\begin{aligned} [\mathbf{B}_{PQ}]_{3(i-1)+k, 3(j-1)+l} &= \int_{S_p} \Phi_{(i)}^{bP}(\mathbf{y}) \int_{S_q} G_{ml}^k(\xi - \mathbf{y}) D_m \Phi_{(j)}^{bQ}(\xi) dS(\xi) dS(\mathbf{y}) \\ &\quad - \int_{S_p} \Phi_{(i)}^{bP}(\mathbf{y}) \int_{S_q} n_r(\xi) H_{rl}^k(\xi - \mathbf{y}) \Phi_{(j)}^{bQ}(\xi) dS(\xi) dS(\mathbf{y}) \end{aligned} \quad (3.20)$$

$$[\mathbf{C}_{PQ}]_{3(i-1)+k, 3(j-1)+l} = \int_{S_p} D_t \Phi_{(i)}^{bP}(\mathbf{y}) \int_{S_q} C_{ml}^{tk}(\xi - \mathbf{y}) D_m \Phi_{(j)}^{bQ}(\xi) dS(\xi) dS(\mathbf{y}) \quad (3.21)$$

$$[\mathbf{D}_a]_{3(i-1)+k, 3(j-1)+l} = \frac{1}{2} \int_{S_a} \delta_{kl} \Phi_{(i)}^{ba}(\mathbf{y}) \Phi_{(j)}^{ba}(\mathbf{y}) dS(\mathbf{y}) \quad (3.22)$$

and the load vectors \mathbf{R}_3 , \mathbf{R}_4 , \mathbf{R}_5 and \mathbf{R}_6 are obtained directly from the discretization of the linear integral operators \mathcal{R}_u , \mathcal{R}_t , \mathcal{R}_c and \mathcal{R}_a defined by (2.37)-(2.40). To construct all involved coefficient matrices, special quadrature rules proposed by Li et al. (1998) are adopted to evaluate both weakly singular and nearly singular integrals and an efficient interpolation-based algorithm similar to that proposed by Rungamornrat and Mear (2008) is implemented to calculate all involved fundamental solutions for generally anisotropic materials.

The final system of linear algebraic equations resulting from the discretization of the governing equations (2.50)-(2.55) takes the following form

$$\begin{bmatrix}
 \mathbf{0} & \mathbf{0} & \mathbf{0} & \mathbf{0} & \mathbf{C}_1 & \mathbf{C}_2 \\
 \mathbf{0} & \mathbf{0} & \mathbf{0} & \mathbf{C}_3 & \mathbf{C}_4 & \mathbf{C}_5 \\
 \mathbf{A}_{uu} & \mathbf{B}_{ut} & \mathbf{B}_{uc} & \mathbf{B}_{ua} & \mathbf{A}_{ua} & \mathbf{0} \\
 \mathbf{B}_{ut}^T & \mathbf{C}_{tt} & \mathbf{C}_{tc} & \mathbf{C}_{ta} & \mathbf{B}_{at}^T & \mathbf{0} \\
 \mathbf{B}_{uc}^T & \mathbf{C}_{tc}^T & \mathbf{C}_{cc} & \mathbf{C}_{ca} & \mathbf{B}_{ac}^T & \mathbf{0} \\
 \mathbf{B}_{ua}^T & \mathbf{C}_{ta}^T & \mathbf{C}_{ca}^T & \mathbf{C}_{aa} & \mathbf{B}_{aa}^T + \mathbf{D}_a & \mathbf{0}
 \end{bmatrix}
 \begin{bmatrix}
 \mathbf{T}^{bu} \\
 \mathbf{U}^{bt} \\
 \Delta \mathbf{U}^{bc} \\
 \mathbf{U}^{ba} \\
 \Sigma^a \\
 \mathbf{U}^p
 \end{bmatrix}
 =
 \begin{bmatrix}
 \mathbf{R}_1 \\
 \mathbf{R}_2 \\
 \mathbf{R}_3 \\
 \mathbf{R}_4 \\
 \mathbf{R}_5 \\
 \mathbf{R}_6
 \end{bmatrix}
 \quad (3.23)$$

The numerical solution of the linear system (3.23) can be obtained from various types of linear solvers such as Gaussian elimination and LU-decomposition methods, the bi-conjugate gradient stabilized method (e.g., Gutknecht, 1993; Y. Saad, 2003; Van der Vorst, 1992) and generalized minimal residual method (e.g., Saad and Schultz, 1986).



3.3 POST-PROCESS FOR STRESS INTENSITY FACTORS

The SIFs along the crack front are to be extracted directly from the solved relative crack-face displacement. Due to the use of special crack-tip elements in the approximation of $\Delta \mathbf{u}^b$ in the neighborhood of the crack front, it allows ones to adopt the explicit formula proposed by Rungamornrat and Mear (2008) to obtain the SIFs. In such calculations, it is only required, in addition to the solved data $\Delta \mathbf{u}^b$, the geometry of the crack and properties of materials constituting the cracked body.

The explicit expression for the stress intensity factors in terms of the solved nodal data along the crack front is given by

$$k_i(\mathbf{x}_c) = \sqrt{\frac{\pi}{2\gamma}} B_{il} [\mathbf{u}^0(\mathbf{x}_c) \cdot \bar{\mathbf{e}}_l(\mathbf{x}_c)] \quad (3.24)$$

where $\{k_2, k_1, k_3\}$ denote mode-I, mode-II, and mode-III stress intensity factors, respectively; \mathbf{x}_c denotes a point along the crack front; $\{\bar{\mathbf{e}}_1, \bar{\mathbf{e}}_2, \bar{\mathbf{e}}_3\}$ denote orthonormal base vectors forming the local Cartesian coordinate system $\{\bar{x}_1, \bar{x}_2, \bar{x}_3\}$ with the origin at \mathbf{x}_c as shown in Figure 3.1; and

$$B_{il} = \frac{1}{2\pi} \int_0^{2\pi} [(\mathbf{a}, \mathbf{a})_{il} - (\mathbf{a}, \mathbf{b})_{im} (\mathbf{b}, \mathbf{b})_{mn}^{-1} (\mathbf{b}, \mathbf{a})_{nl}] d\beta \quad (3.25)$$

CHAPTER 4

NUMERICAL RESULTS AND DISCUSSIONS

This chapter consists of two main parts. The first part devotes directly to the verification of the proposed technique and the convergence of numerical solutions whereas the second part involves the application of the verified technique to study the influence of certain parameters on the stress intensity factors along the crack front of cracked bodies after repaired.

4.1 VERIFICATIONS



In this section, results from the analysis of several representative problems by the proposed technique are reported. Both embedded and surface breaking cracks are considered. In the analysis, 6-node triangular elements and 8-node quadrilateral elements are employed to discretize the patch, the adhesive layer, the boundary of the cracked body, and the majority of the crack surface. The remaining portion of the crack surface adjacent to the crack front is discretized by 9-node special crack-tip elements. To investigate the convergence of numerical solutions, three meshes representing coarse, intermediate, and fine discretizations are adopted in the analysis of each problem and obtained results are then compared. To confirm the correctness of the implemented technique, generated numerical solutions are also compared with reliable benchmark solutions. In addition, some of the representative problems are chosen to be relatively complex to further demonstrate the capability and computational robustness of the proposed technique.

4.1.1 Strengthening of cube containing near surface crack

Consider a cube of an isotropic linearly elastic material that occupies the region $[-w, w] \times [-w, w] \times [-w, w]$ in space and contains a penny-shaped crack of radius a as shown schematically in Figure 4.1. The crack surface lies on a plane $x_3 = 0$ with its center located at a point $(0.4w, 0, 0)$. The crack front can be parametrized in terms of the angular position $\theta \in [0, 2\pi]$ by

$$x_1 = 0.4w - a \cos \theta, \quad x_2 = a \sin \theta, \quad x_3 = 0 \quad (4.1)$$

The cube is loaded by a uniform normal traction $t_3 = \sigma_0$ on the face $x_3 = w$ and the uniform normal traction $t_3 = -\sigma_0$ on the face $x_3 = -w$. To strengthen the cracked body, a patch of uniform thickness h_p is bonded to its entire face $x_1 = w$ by the adhesive layer of uniform thickness h^a . In the numerical study, the aspect ratio $a/w = 0.5$ and Young's modulus and Poisson's ratio given in Table 4.1 are considered and three meshes shown in Figure 4.2 are adopted.

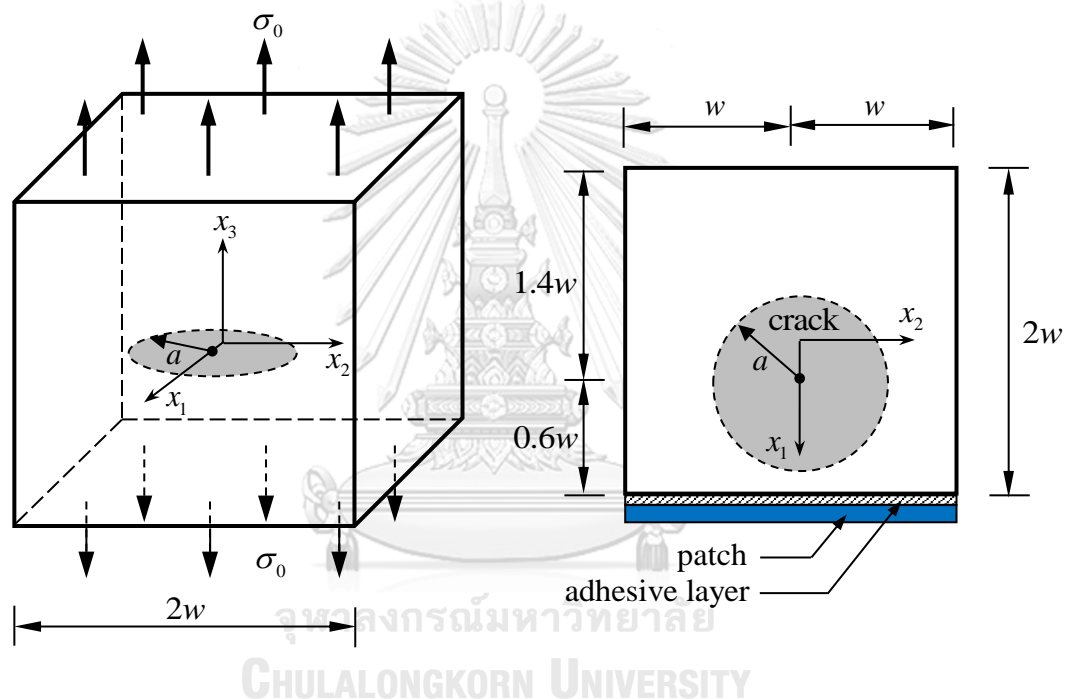


Figure 4.1. A cube containing near-surface penny-shaped crack strengthened by adhesively bonded patch.

Table 4.1. Material properties for cracked body, patch, and adhesive layer

Materials	Young's modulus ($\times 10^6$ psi)	Poisson's ratio
Cracked body	2.0	0.25
Patch	17.4	0.25
Adhesive layer	0.1	0.33

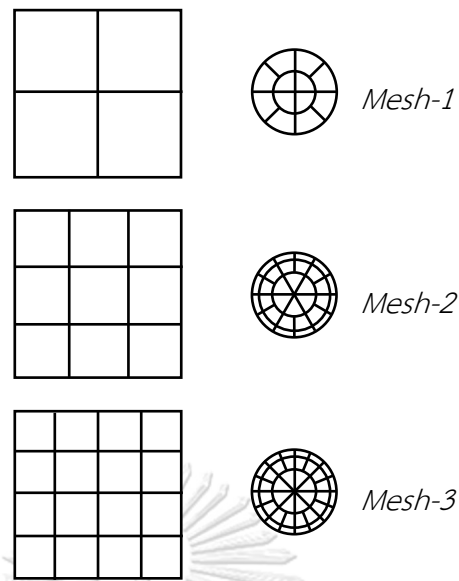


Figure 4.2. Three meshes used in numerical simulations (only mesh of each face of cube is shown and it is identical to those for patch and adhesive layer).

Since the analytical solution for this particular problem is not available in the literature, the reference solution constructed from the standard finite element technique is employed in the verification process. To ensure that the finite element solution is of good quality, a series of three different meshes adopted as shown in Figure 4.3 is utilized in the analysis and results for the stress intensity factors along the crack front of a cracked body with and without the strengthening are reported in Figure 4.4. It is obviously seen that a significant amount of degrees of freedom is required, for the finite element method, to arrive at the converged solution. As become evident later that the proposed technique is more computationally efficient in the sense that relatively few degrees of freedom are needed to generate numerical solutions of the comparable quality. The solution obtained from the finest mesh is then used as the benchmark solution. Finally, it is remarked that the same procedure described here is also employed throughout to construct the benchmark solution for all problems investigated.

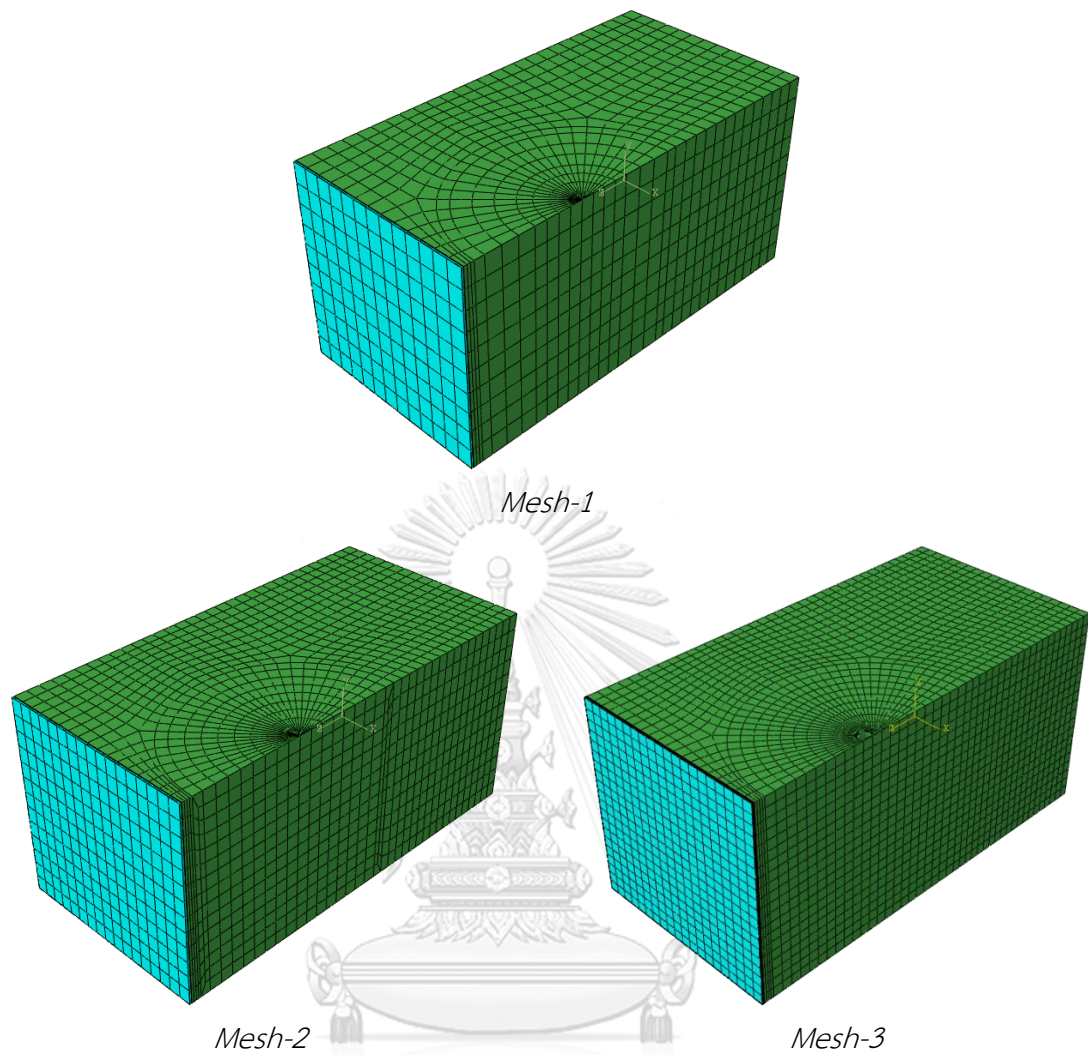


Figure 4.3. Three meshes adopted to investigate convergence of finite element solutions: Mesh-1 containing 6,930 elements, Mesh-2 containing 13,982 elements, and Mesh-3 containing 43,400-elements.

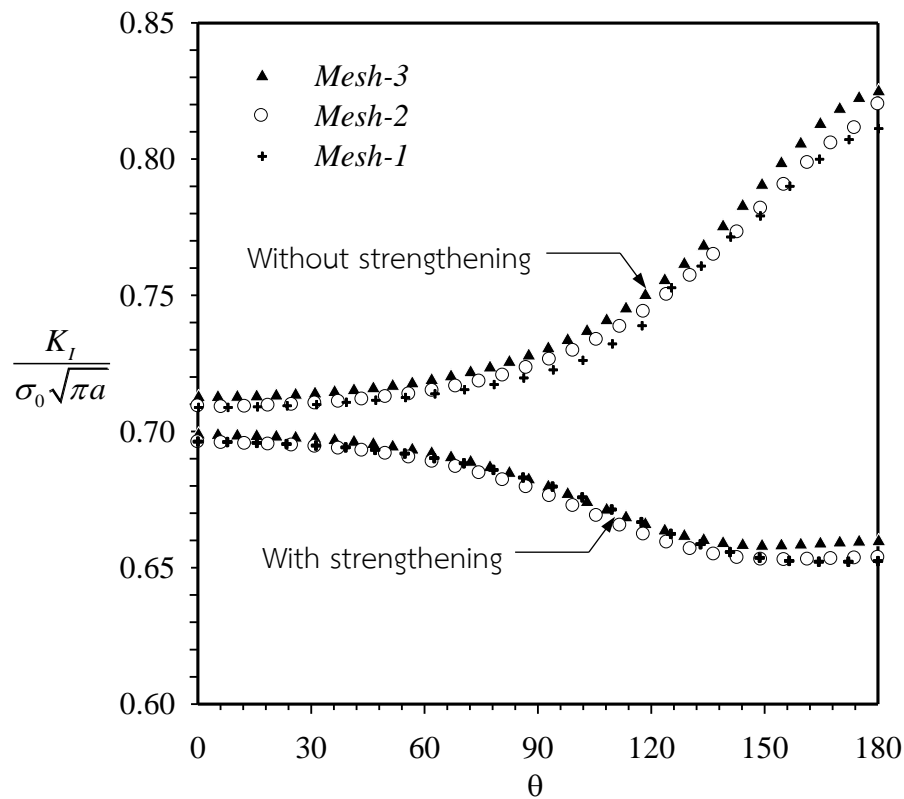


Figure 4.4. Normalized mode-I stress intensity factor of a near-surface penny-shaped crack embedded in a cube which is subjected to normal traction σ_0 . Results are generated by a reliable finite element program and those associated with the case of strengthening are reported for $h^a/w=0.001$ and $h_p/w=0.01$.

Due to the symmetry and loading conditions considered, only the mode-I stress intensity factor (K_I) is non-zero. The normalized K_I obtained from the three meshes are reported in Figure 4.5 together with those generated by a reliable finite element program for the cases with and without the strengthening. As can be seen from this set of results, numerical solutions converge as the mesh is refined and the excellent agreement between the converged and reference solutions (with the difference within a fraction of 1%) is clearly observed. Note in particular that the relatively coarse meshes such as the Mesh-1 (containing only 12 elements on the crack surface) and Mesh-2 (containing only 30 elements on the crack surface) can also yield quite accurate results; this is due mainly to the use of 9-node special crack-tip elements in the enhancement of the approximation of the near-front relative crack-face displacement. After the cracked body is strengthened by the

adhesively bonded patch (with $h^a / w = 0.001$ and $h_p / w = 0.01$), the stress intensity factor is significantly reduced especially in the region near the bonded patch where the reduction from the unrepaired case is up to 20%.

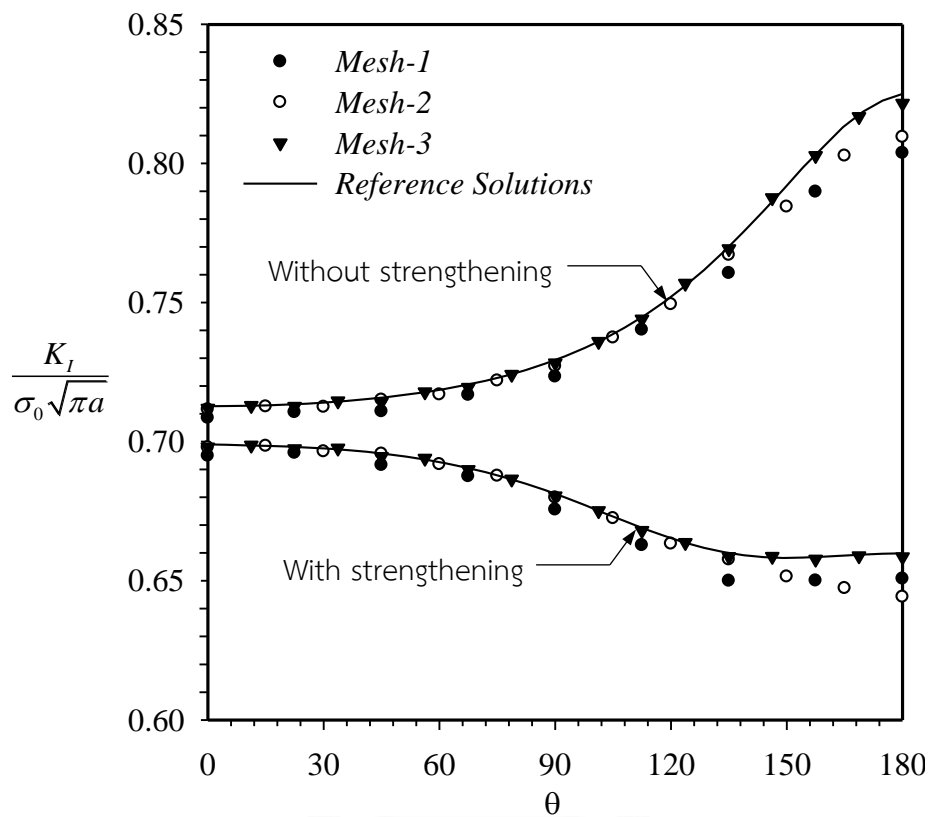


Figure 4.5. Normalized mode-I stress intensity factor of a near-surface penny-shaped crack embedded in a cube which is subjected to normal traction σ_0 . Results for the case of strengthening are reported for $h^a / w = 0.001$ and $h_p / w = 0.01$.

4.1.2 Plate containing centered through crack

Next, consider a rectangular plate of thickness t and containing a centered through crack of length $2c$ as illustrated in Figure 4.6. The crack is contained in a plane $x_3 = 0$ and the plate is loaded by a uniformly distributed normal traction σ_0 at its top and bottom surfaces. The cracked plate is repaired by a pair of patches with a uniform thickness h_p and dimensions $2d \times 2e$. The patches are installed to cover the surface-breaking lines (located on the surfaces $x_1 = 0.5t$ and $x_1 = -0.5t$ of the plate) by the adhesive material of uniform thickness h^a as indicated in Figure 4.6. In the

analysis, the following parameters and aspect ratios $h^a/t=0.001$, $h_p/t=0.01$, $d/c=0.75$, $e/c=1.47$, $c/t=1$, $b/c=2$, and $h/b=2$ are considered; three meshes shown in Figure 4.7 are adopted; and the material properties given in Table 4.1 are employed.

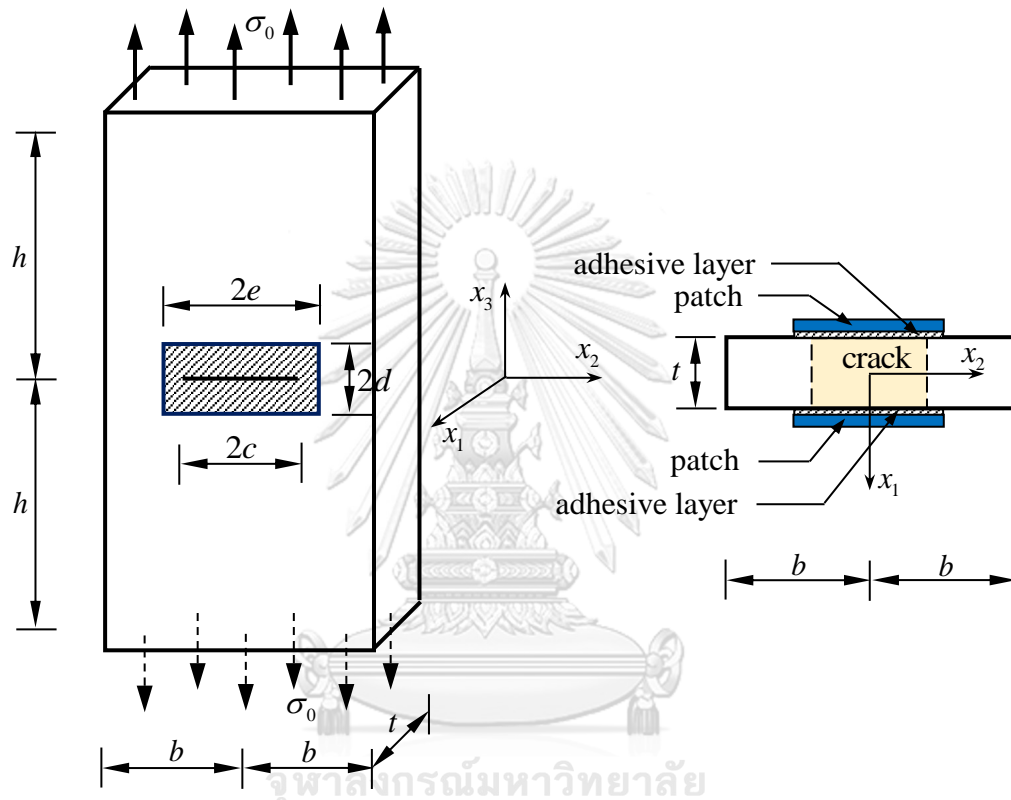


Figure 4.6. Schematic of rectangular plate containing a centered through crack and repaired by a pair of adhesively bonded patches.

The converged finite element solution can be also constructed by following the same procedure as that employed in the previous problem and the final finite element mesh is also demonstrated in Figure 4.8.

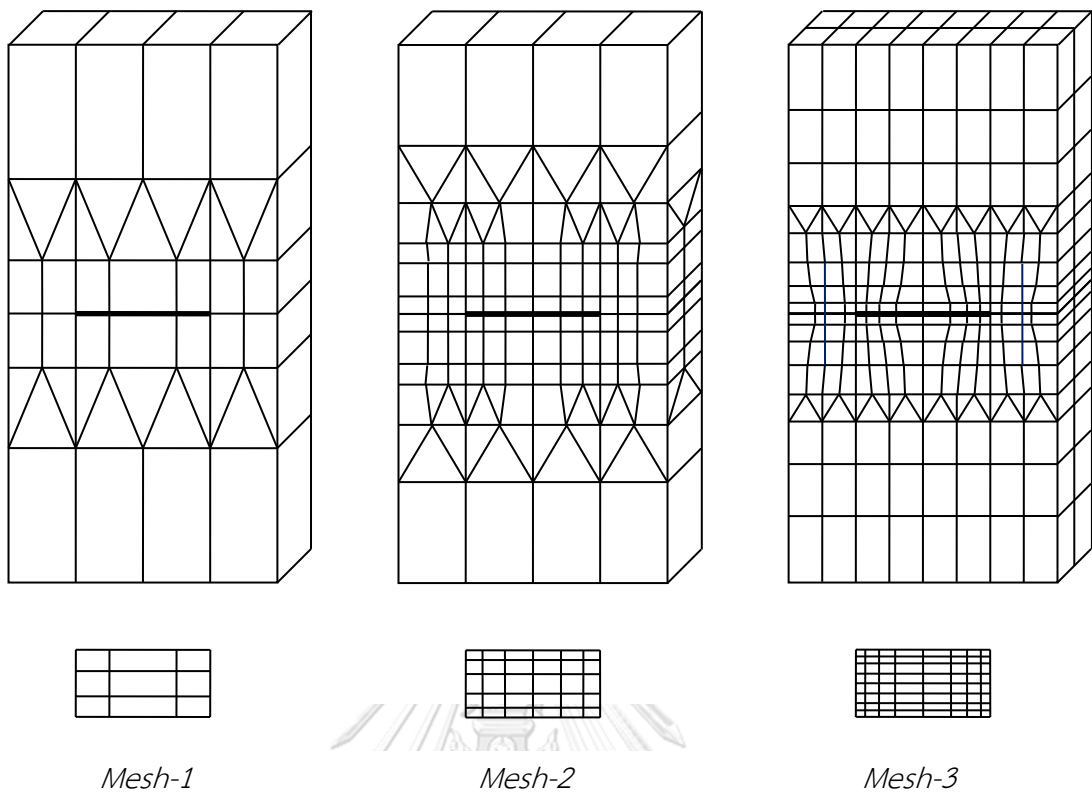


Figure 4.7. Three meshes adopted in analysis. Meshes of crack are shown below those of boundary.

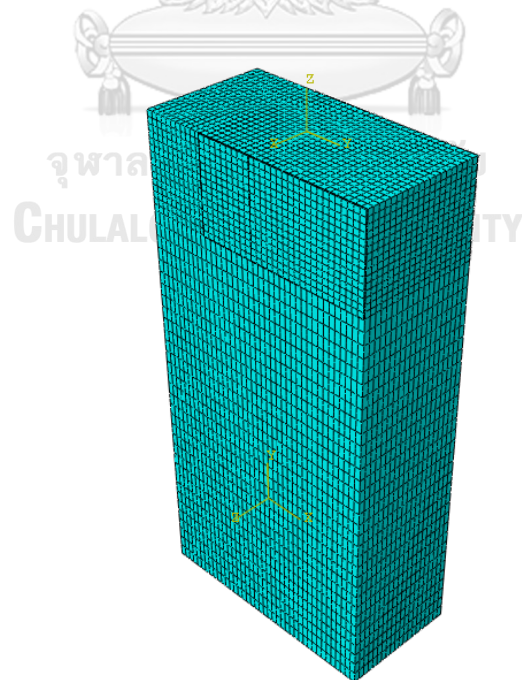


Figure 4.8. A final mesh (containing 51,450 elements) used to generate converged finite element solution. Mesh is shown only for a quarter of the whole cracked body.

Computed mode-I stress intensity factors from the three meshes are normalized and reported in Figure 4.9 as a function of the arc length s measured from the center of the crack front for the cases with and without the repair. It is seen that upon the mesh refinement, the numerical solutions exhibit an excellent convergence behavior and only slight dependence on the level of discretization is observed. In particular, the coarsest mesh with the relatively low number of degrees of freedom especially for a region close to the crack can still yield stress intensity factors comparable to the converged solution. It is also found by comparing the converged results with the reference solutions generated from a finite element technique that the two solutions are almost indistinguishable for both repaired and unrepaired cases. After the cracked plate is repaired, the stress intensity factor drops significantly especially in the regions near the bonded patches. For this particular repair configuration (of both patches and adhesive layers), the reduction of the stress intensity factor is not less than 40% for the entire crack front.

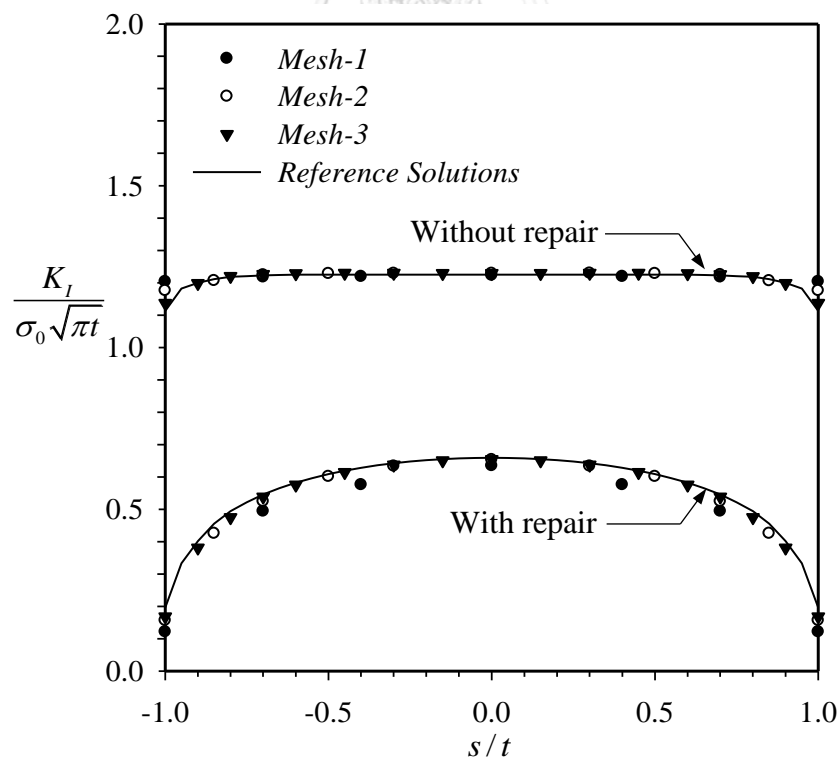


Figure 4.9. Normalized mode-I stress intensity factor for a rectangular plate containing centered through crack under normal traction σ_0 with and without repair.

4.1.3 Plate containing surface-breaking semi-elliptical crack

Consider, next, a rectangular plate of dimensions $2h \times 2b \times t$ and containing a surface-breaking semi-elliptical crack as depicted in Figure 4.10. The crack is contained in the plane $x_3 = 0$ with the crack front being parametrized by

$$x_1 = t/2 - a \sin \theta, \quad x_2 = c \cos \theta, \quad x_3 = 0 \quad (4.2)$$

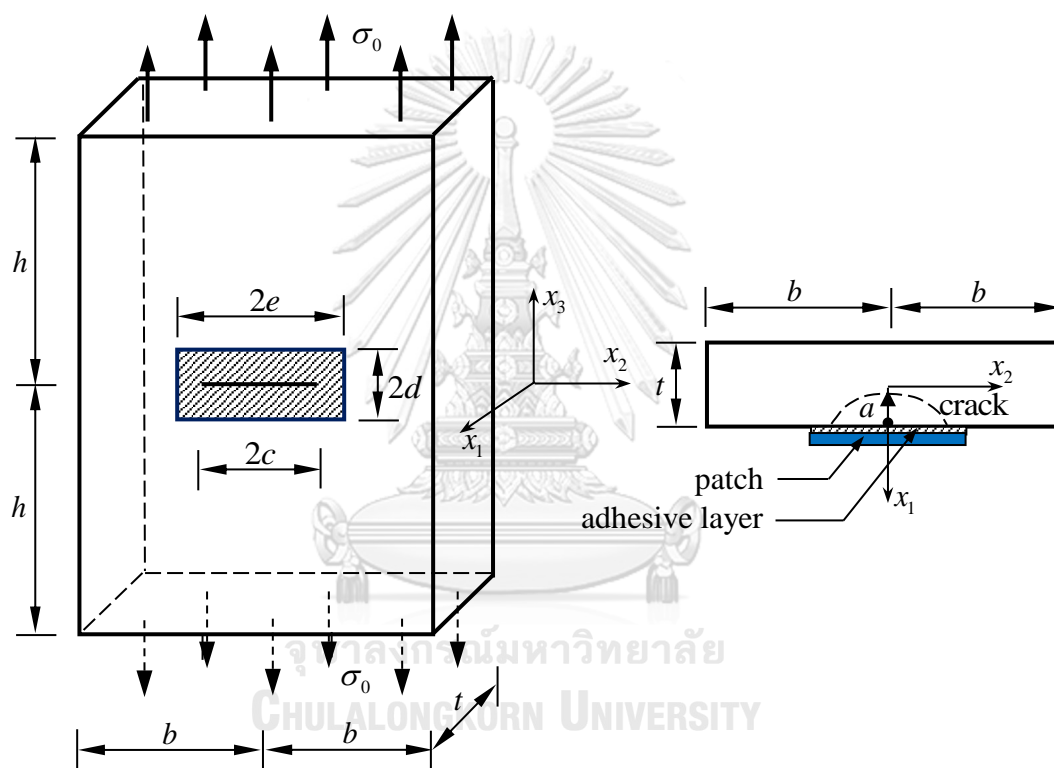


Figure 4.10. Schematic of rectangular plate containing surface-breaking, semi-elliptical crack and repaired by adhesively bonded patch.

where a and c denote the minor and major semi-axes, respectively, and $\theta \in [0, \pi]$ denotes the angular position along the crack front. The plate is subjected to a uniformly distributed normal traction σ_0 on its upper and lower faces. To repair the cracked body, a patch of uniform thickness h_p and dimensions $2d \times 2e$ is bonded to the face $x_1 = 0.5t$ of the plate to cover the entire surface breaking line by means of

the adhesive layer of uniform thickness h^a . Dimensions of the plate, crack, patch, and adhesive layer are taken such that $h^a/t=0.002$, $h_p/t=0.02$, $d/c=0.5$, $e/c=1.25$, $a/t=0.4$, $c/a=5$, $b/c=5$ and $h/b=1$, and Young's modulus and Poisson's ratio for each material are given in Table 4.1. Three meshes shown in Figure 4.11 are employed in the simulations. It is worth noting that this representative problem for the unrepaired case and the three meshes adopted are identical to those reported in the work of Rungamornrat and Mear (2008).

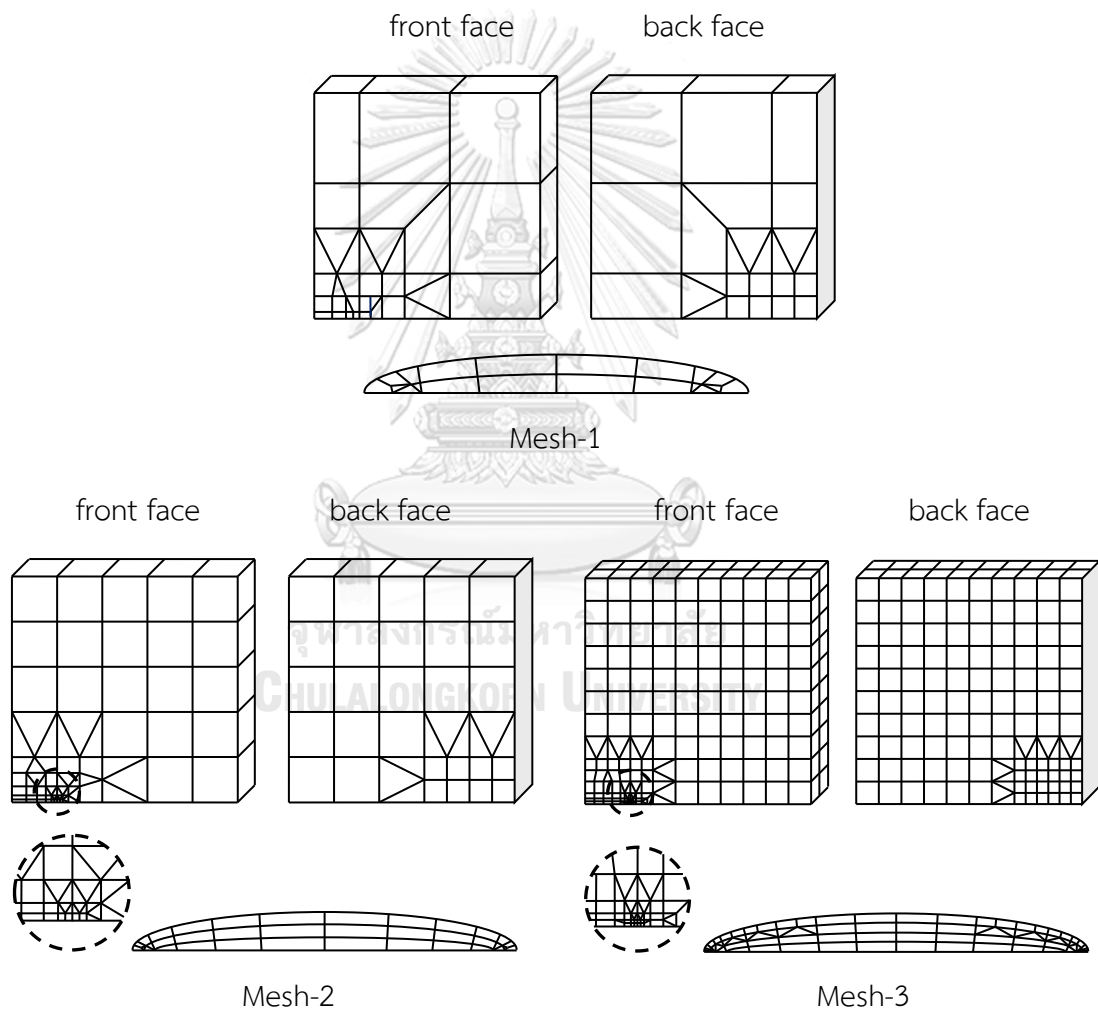


Figure 4.11. Three meshes adopted in the analysis of a rectangular plate containing surface-breaking, semi-elliptical crack. The entire crack mesh and only one quarter of the outer boundary mesh are shown.

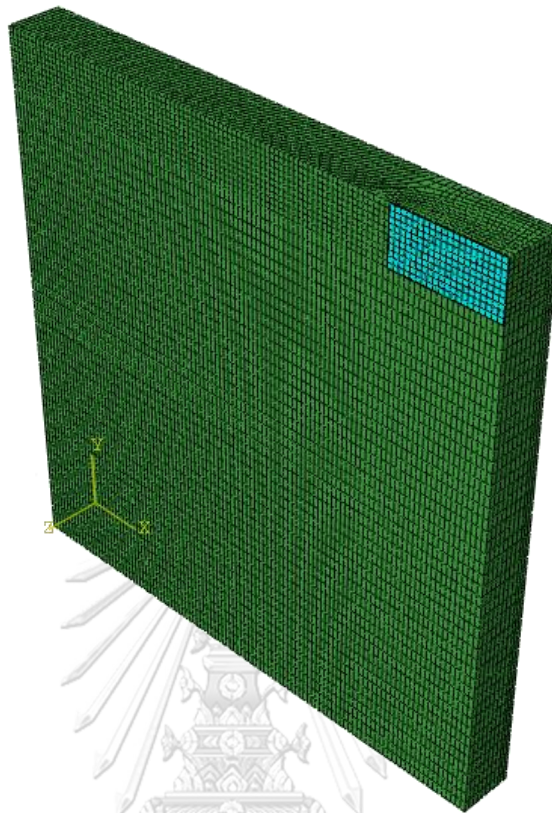


Figure 4.12. A final mesh (containing 62,510 elements) used to generate converged finite element solution. Mesh is shown only for a quarter of the whole cracked body.

Due to the symmetry of the plate, crack, repair configurations, and loading conditions with respect to the plane of the crack, only mode-I stress intensity factor does not vanish along the crack front. The normalized mode-I stress intensity factors generated by the three meshes, for both repaired and unpaired cases, are shown in Figure 4.13 together with results generated by a finite element program with the mesh shown in Figure 4.12. Again, it is observed that the convergence of the numerical solutions is achieved as the mesh is refined. In particular, results from the Mesh-2 and Mesh-3 are only slightly different whereas that from the Mesh-1 is quite different from the converged solution since the mesh is too coarse to accurately capture the relatively complex response. The validity of the implemented technique is also confirmed by the good agreement between the converged and reference solutions indicated in Figure 4.13. It can be also remarked that after the cracked

plate is repaired by the adhesively bonded patch with the specified repair configuration and properties, the stress intensity factor can be reduced at least by half for the entire crack front.

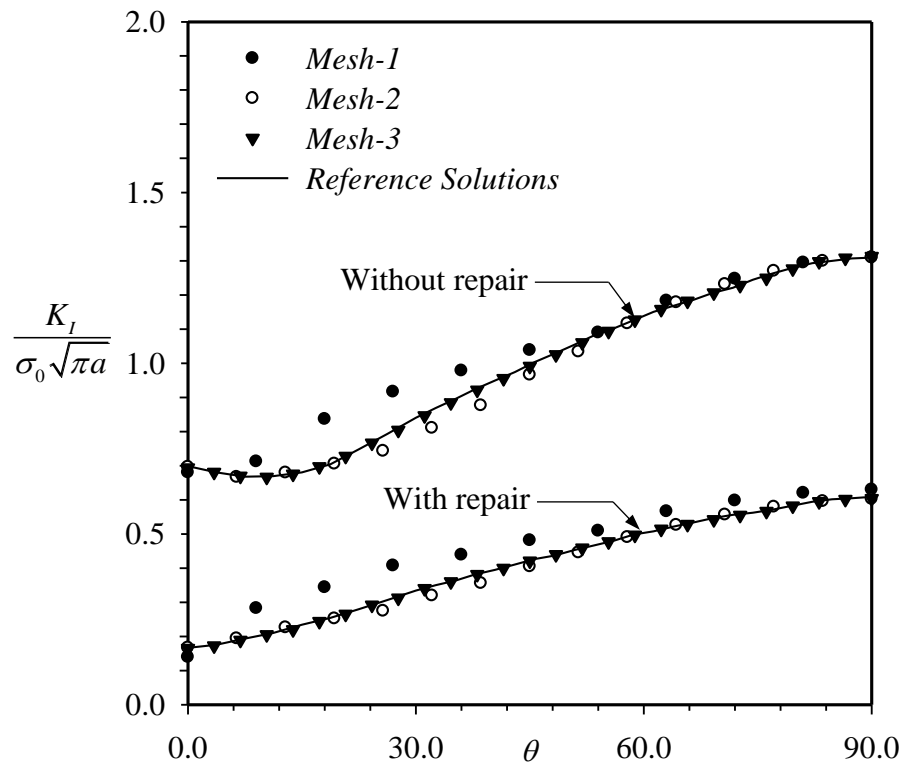


Figure 4.13. Normalized mode-I stress intensity factors for rectangular plate containing surface-breaking, semi-elliptical crack under normal traction σ_0 .

4.1.4 Edge cracked bar

As a final example, consider a rectangular bar containing a through-the-thickness, surface-breaking crack as shown schematically in Figure 4.14. This cracked body is subjected to a uniformly distributed normal traction σ_0 on the upper and lower surfaces of the bar. To repair this cracked bar, three patches of the uniform thickness h_p are attached to the bar, by the adhesive layer of uniform thickness h^a , to fully cover the surface breaking line as clearly illustrated in the figure. In the simulations, the geometry of the bar, crack, patch, and adhesive layer is taken such that $h^a/t = 5 \times 10^{-4}$, $h_p/t = 5 \times 10^{-3}$, $w/t = 0.75$, $h/t = 0.875$, $a/t = 0.5$, $d/t = 0.2$,

$e/t = 0.675$, and three meshes shown in Figure 4.15 and material properties given in Table 4.1 are employed.

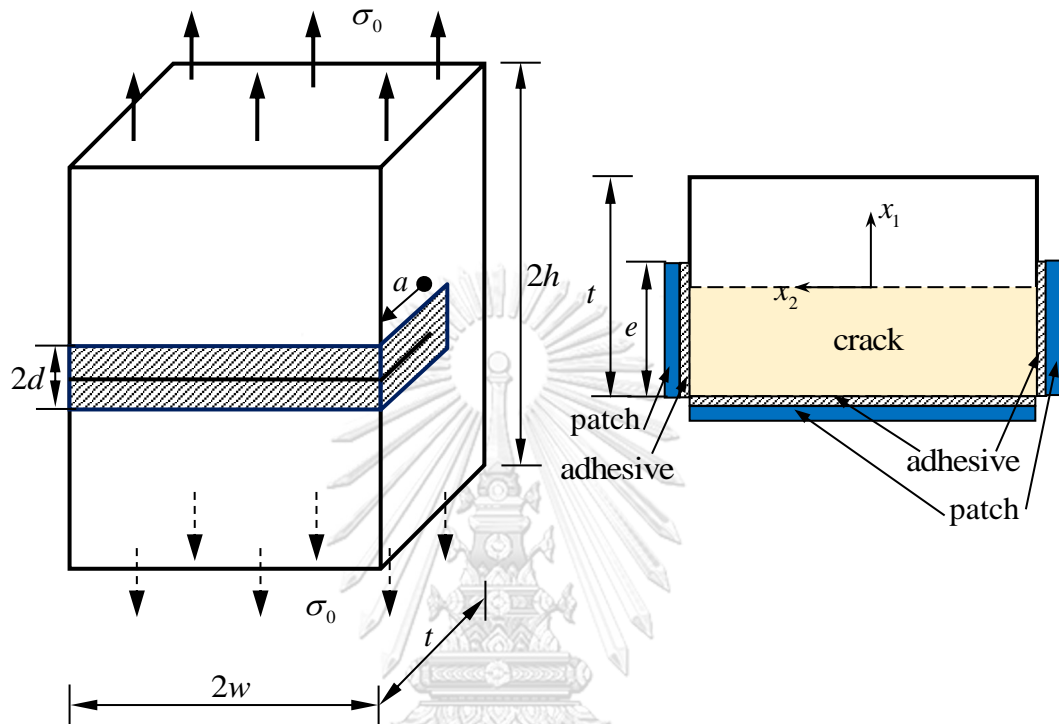


Figure 4.14. Schematic of a rectangular bar containing a through-the-thickness, surface-breaking crack under uniformly distributed normal traction and repaired by adhesively bonded patches.

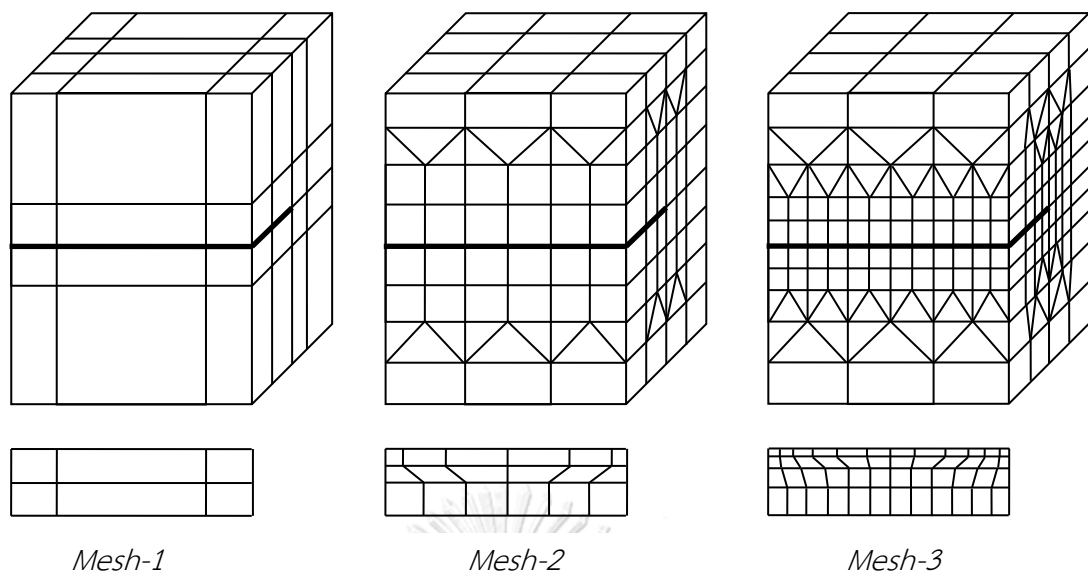


Figure 4.15. Three meshes for rectangular bar containing a through-the-thickness, surface-breaking crack. Mesh for the crack mesh is shown below that of the boundary.

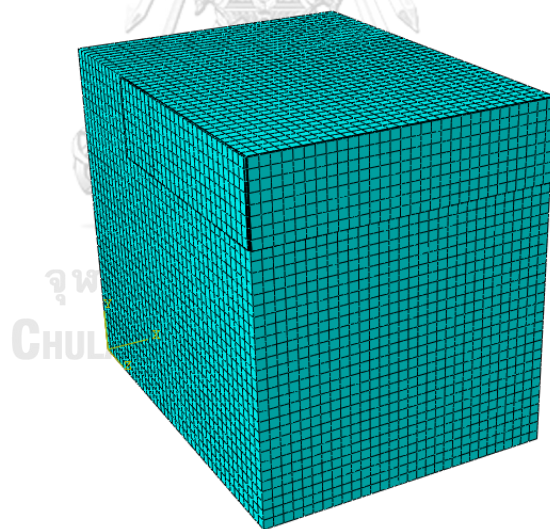


Figure 4.16. A final mesh (containing 48,840 elements) used to generate converged finite element solution. Mesh is shown only for a quarter of the whole cracked body.

The loading condition and the configurations of the cracked body and the repair gives rise to pure mode-I stress intensity factor along the crack front. Numerical results for this essential fracture data are reported in Figure 4.17 as a function of the arc length s measured from the center of the crack front for the three meshes and

both repaired and unrepaired cases. It is seen from this set of results that the stress intensity factors generated from the intermediate and fine meshes (i.e., Mesh-2 and Mesh-3, respectively) are nearly identical except in a region very near the vertices (i.e., points where the crack front intersects the boundary) where the solution tends to drop rapidly to zero. Even the coarsest mesh (i.e., Mesh-1), which utilizes only three special crack-tip elements along the crack front, can still capture the distribution of the stress intensity factor quite accurately. This, as a result, confirms the convergence of the numerical results and the slight dependence of the solution on the level of discretization. Furthermore, the implemented technique is additionally verified by comparing the converged results with the reference solution generated by a finite element program with the mesh shown in Figure 4.16 and the good agreement of the two solutions is concluded. As can be seen from Figure 4.17, the patching repair can significantly reduce the stress intensity factor for the whole crack front. For a particular repair configuration considered here, the reduction of the stress intensity factor along the crack front is at least 65%.

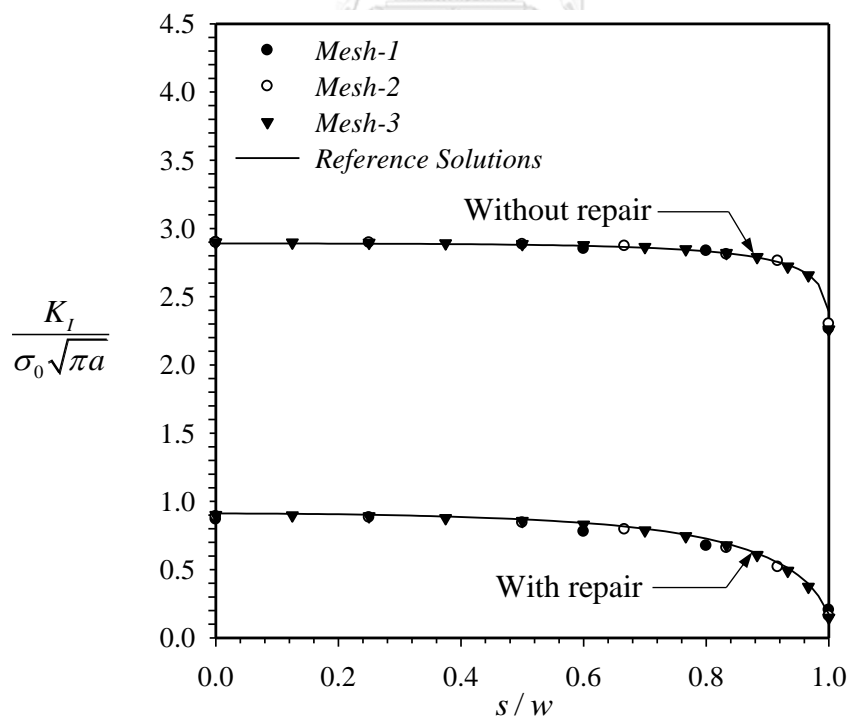


Figure 4.17. Normalized mode-I stress intensity factor for rectangular bar containing through-the-thickness, surface-breaking crack under uniformly distributed normal traction σ_0 .

4.2 PARAMETRIC STUDY

In this section, a fully tested numerical technique is utilized as an analysis tool to study the influence of the stiffness of the patch (defined by $E^p h_p$, where E^p and h_p are Young's modulus and thickness of the patch) and the shear stiffness of the adhesive layer (defined by G^a / h^a where G^a and h^a are the shear modulus and the thickness of the adhesive layer) on the reduction of the stress intensity factors along the crack front. This piece of information can be potentially useful in the selection of both patches and adhesive layers not only to confine the stress intensity factors below the specified tolerance in order to prevent the subsequent crack growth but also to attain optimal repair design. Three cracked bodies shown in Sections 4.1.2-4.1.4 including the plate containing a centered through crack, the plate containing surface-breaking semi-elliptical crack, and the edge cracked bar are chosen as the representative cases in the parametric study. To ensure the accuracy of computed solutions, the finest mesh for each case is employed in the simulations.

4.2.1 Plate containing centered through crack

Consider the cracked plate shown in Figure 4.6. In the numerical study, dimensions of the plate, the crack, and the size of the patch are maintained such that $d/c=0.75$, $e/c=1.47$, $c/t=1$, $b/c=2$, and $h/b=2$ and the load level remains unchanged. Properties of the material constituting the cracked plate are taken from Table 4.1.

First, consider the cracked plate repaired by following four different types of patches including Aluminum, S45C, Si3N4 and Laminate 460/1500. The material properties of those patches are given in Table 4.2. In the simulations, the thickness of the patch and the adhesive layer is taken as $h_p/t=0.01$ and $h^a/t=0.001$ and the material properties for the adhesive layer are taken from Table 4.1. The normalized stress intensity factors along the crack front, after the repair, are reported in Figure 4.18 together with the unrepaired case. As expected, the reduction of the stress intensity factors from the unrepaired case decreases as Young's modulus of the

material constituting the patch increases. The increase in Young's modulus obviously enhances the stiffness $E^p h_p$ of the patch.

Table 4.2. Material properties for different types of patches (e.g., Liu and Xu, 2000; Jiann-Quo and Kam-Lun, 1991; Yu et al., 2014)

Materials	Young's modulus (GPa)	Poisson's ratio
Aluminum	71.02	0.32
S45C	206	0.3
Si3N4	304	0.27
Laminate 460/1500	477	0.25

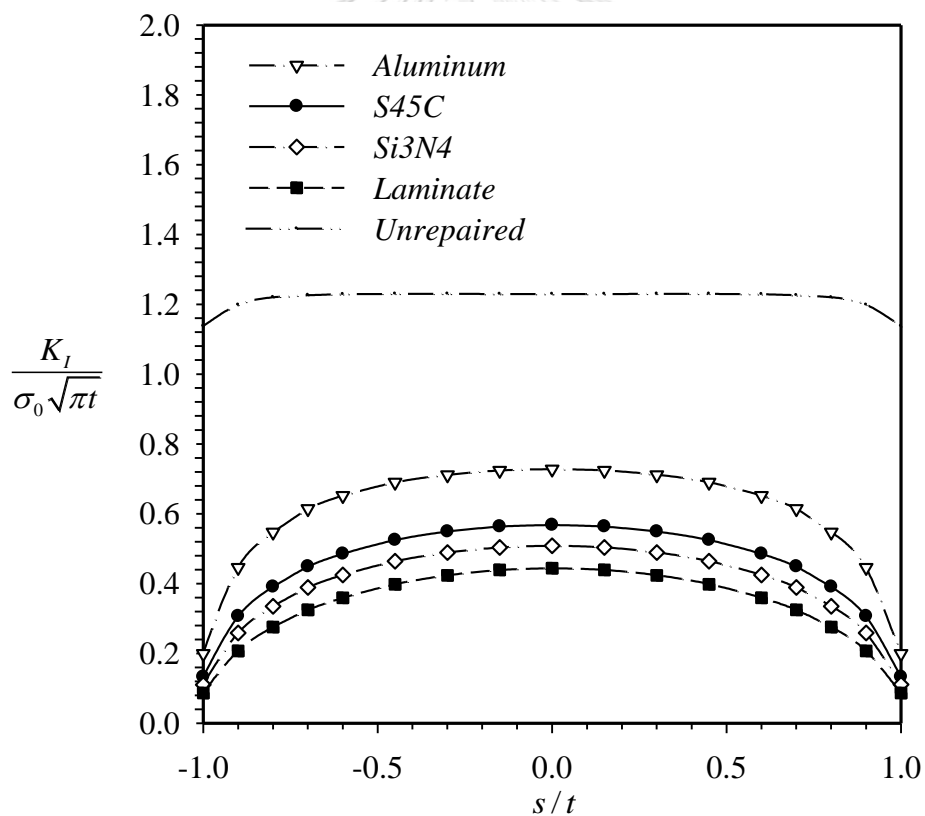


Figure 4.18. Normalized mode-I stress intensity factors along the crack front for plate containing centered through crack after repaired by four different types of patches.

To clearly understand the influence of the stiffness of the patch on the reduction of the stress intensity factor (SIF) along the crack front, simulations are

carried out for various values of the patch stiffness $E^p h_p$, while maintaining all other parameters of the cracked body and the adhesive layers. The percent of reduction of the SIF from the unrepaired case at four different points along the crack front (i.e., $s/t \in \{0, 0.3, 0.6, 0.9\}$) are reported versus the normalized patch stiffness $E^p h_p / E^b t$ where E^b denotes Young's modulus of the material constituting the cracked plate in Figure 4.19. Results at values of $E^p h_p / E^b t$ coincident with the four different types of patch shown in Table 4.2 are also marked in this plot. It is seen from this set of results that as the stiffness of the patch increases, the percent reduction of the SIF at four selected points along the crack front from the unrepaired case increases monotonically and finally converges to a certain limit when the stiffness of the patch becomes infinite (i.e., the patch becomes rigid). The latter observation simply implies that no further reduction of the stress intensity factors from such the limit can be achieved. Clearly, the SIF along the entire crack front can be reduced, after the repair, as much as 70% relative to the unrepaired case (controlled by the point $s/t = 0$ where the stress intensity factor attains the maximum values). It is worth noting that the rate of reduction of the SIF decreases quite rapidly to zero as the normalized stiffness of the patch $E^p h_p / E^b t$ increases. Therefore, increasing $E^p h_p / E^b t$ beyond a certain range (e.g., 1.0-1.5 for this particular case) does not result in any further significant reduction of the SIF and may render the repair cost ineffective. Results as reported in Figure 4.19 can also be used in the selection of the stiffness of the patch in the repair design to confine the range of the stress intensity factors below the required tolerance.

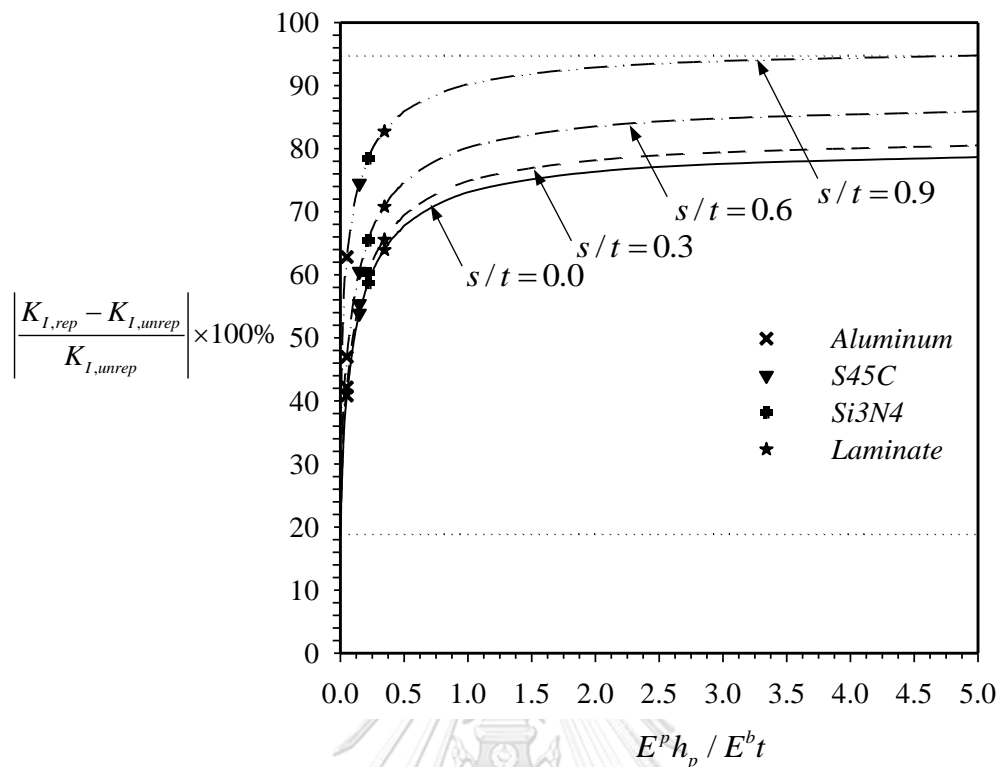


Figure 4.19. Percent reduction of mode-I stress intensity factor relative to unrepaired case at four selected points with $s/t \in \{0, 0.3, 0.6, 0.9\}$ versus normalized stiffness of the patch.

Finally, the influence of the stiffness of the adhesive layer G^a / h^a on the SIF along the crack front is examined. In the simulations, the material properties of the cracked body and the patches are taken from Table 4.1 and the thickness of the patch h_p is held constant at $h_p / t = 0.01$. The percent reduction of the SIF from the unrepaired case at four different points along the crack front (i.e., points associated with $s/t \in \{0, 0.3, 0.6, 0.9\}$) versus the normalized stiffness of the adhesive layer $G^a t / E^b h^a$ are reported in Figure 4.20. In this plot, results at values of $G^a t / E^b h^a$ associated with four different types of adhesive materials with their properties (Young's modulus, shear modulus and Poisson's ratio) given in Table 4.3 are also marked. It is remarked that as the normalized stiffness of the adhesive layer $G^a t / E^b h^a$ approaches zero, the unrepaired case is recovered whereas as $G^a t / E^b h^a$ approaches infinity, obtained results are identical to the case that the patch is perfectly and directly bonded to the cracked body. It is apparent from Figure 4.20 that the reduction of the mode-I stress intensity factor for the entire range of

$G^a t / E^b h^a$ (i.e., $G^a t / E^b h^a \in [0, \infty)$) has the same trend as that observed in Figure 4.19. In particular, the rate of percent reduction is quite rapid for $G^a t / E^b h^a \leq 1$ and quickly decays as the normalized stiffness $G^a t / E^b h^a$ increases. It can be recommended from this observation that if the stiffness of the adhesive layer is chosen to be sufficiently large (larger than 1 for this particular case), it is not necessary to take the adhesive layer into account in the modeling. On the contrary, if $G^a t / E^b h^a$ is relatively small, modeling of the cracked body under the patching repair without integrating the adhesive layer can lead to inaccurate results.

Table 4.3. Material properties for different types of adhesive layers (e.g., Ricci et al., 2011; Rodríguez-Tembleque and Aliabadi, 2016)

Materials	Young's modulus (GPa)	Shear modulus (GPa)	Poisson's ratio
AF163-2K	1.10	0.44	0.34
Cytec FM73	1.43	0.53	0.35
Loctite Hysol EA95	2.48	0.905	0.37
Epoxy	4.08	1.478	0.38

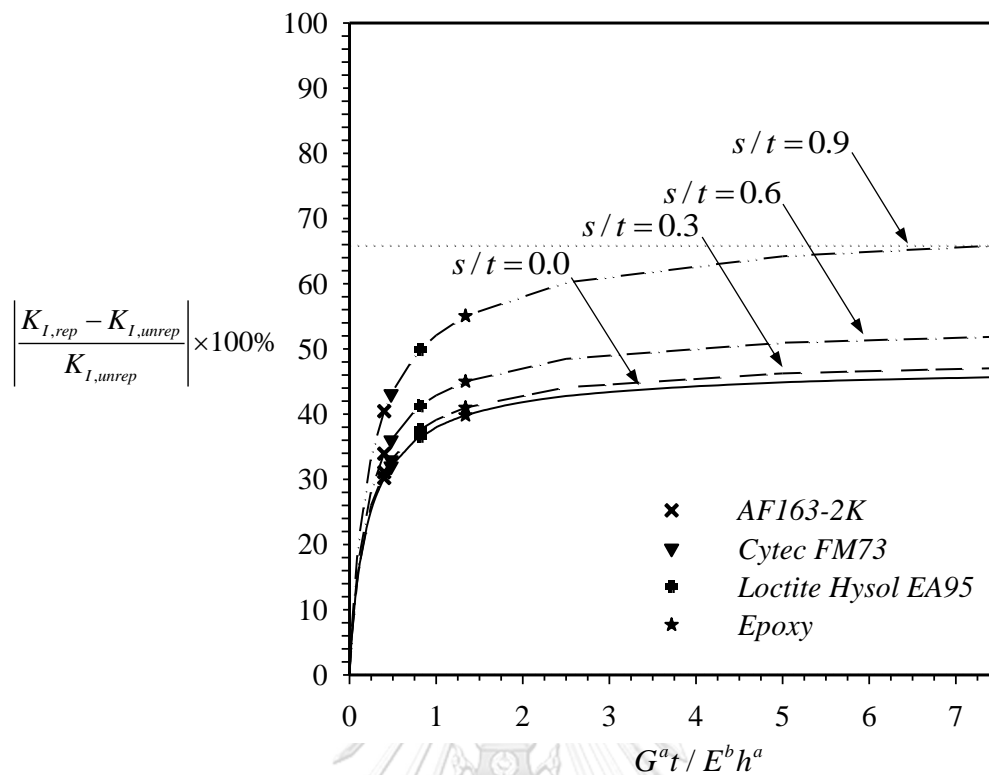


Figure 4.20. Percent reduction of mode-I stress intensity factor relative to unrepaired case at four selected points with $s/t \in \{0, 0.3, 0.6, 0.9\}$ versus normalized stiffness of the adhesive layer.

4.2.2 Plate containing surface-breaking semi-elliptical crack

Next, consider the plate containing the surface-breaking semi-elliptical crack shown in Figure 4.10. In the simulations, geometry of the plate, the crack, and the size of the patch are maintained such that $d/c=0.5$, $e/c=1.25$, $a/t=0.4$, $c/a=5$, $b/c=5$ and $h/b=1$; the loading condition is fixed; and properties of the material constituting the cracked plate are taken from Table 4.1.

The normalized mode-I stress intensity factors along the crack front of the cracked plate repaired by four different types of patches given in Table 4.2 are shown in Figure 4.21. Results are generated for $h_p/t=0.02$ and $h^a/t=0.002$ with the material properties of the adhesive layer taken from Table 4.1. By following the same procedure as that employed in the previous case, the percent reduction of the stress intensity factor from the unrepaired case at four different points along the

crack front (i.e., points associated with $\theta \in \{6.5, 45, 70, 90\}$) can be obtained as a function of the normalized stiffness of the patch $E^p h_p / E^b t$ and the normalized stiffness of the adhesive layer $G^a t / E^b h^a$ as reported in Figures 4.22 and 4.23, respectively. As can be seen from Figure 4.21, as the modulus of a material constituting the patch increases, the patch stiffness increases and this enhances the reduction of the stress intensity factor from the unrepaired case. Results from Figure 4.22 also suggest the suitable range of the patch stiffness for the effective repair and to meet the required tolerance to prevent the subsequent crack advances. In addition, as supported by results in Figure 4.23, the stiffness of the adhesive layer (linearly and inversely proportional to the shear modulus and the layer thickness, respectively) also significantly influences the repair performance. As the stiffness of the layer increases, the effectiveness of the patch as the load sharing element is more apparent.

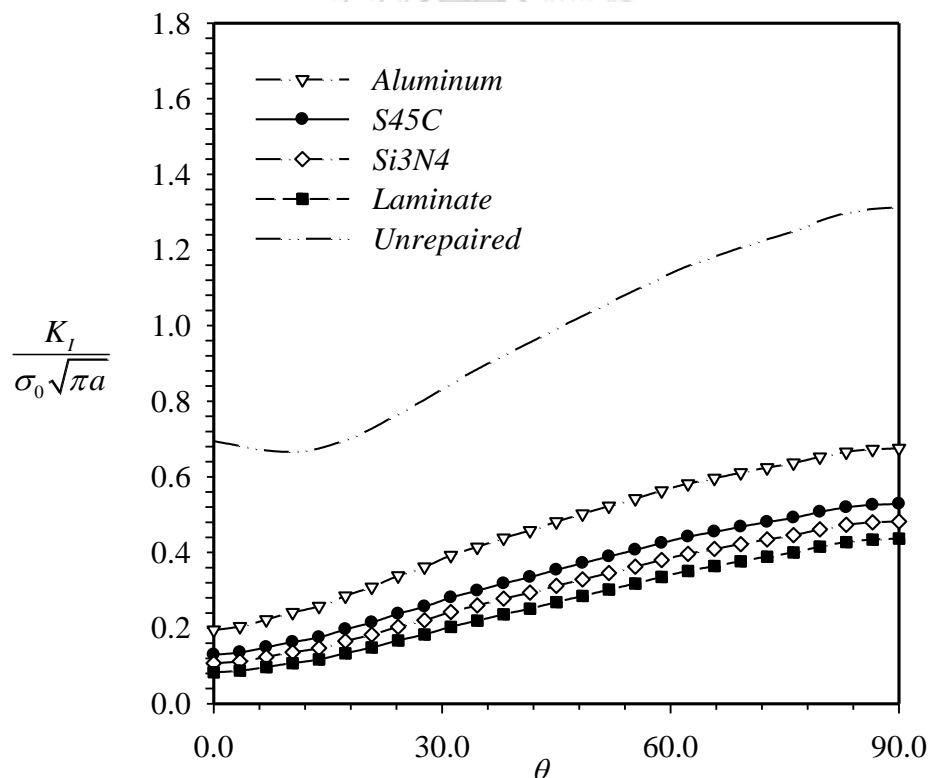


Figure 4.21. Normalized mode-I stress intensity factors along the crack front for plate containing surface-breaking semi-elliptical crack after repaired by four different types of patches.

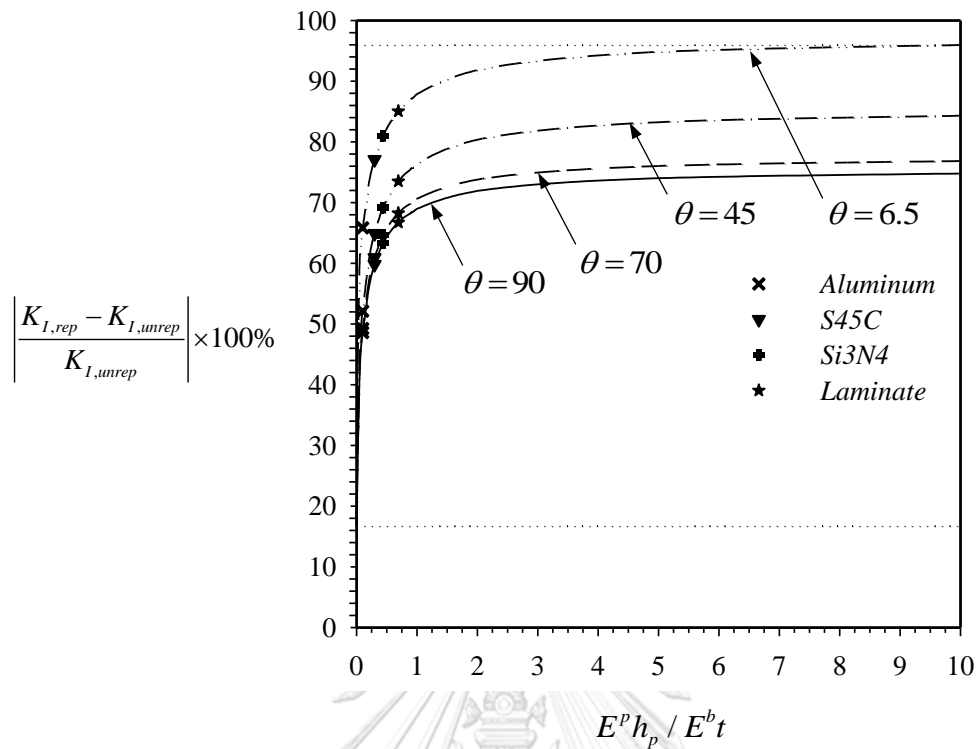


Figure 4.22. Percent reduction of mode-I SIF relative to unrepaired case at four selected points with $\theta \in \{6.5, 45, 70, 90\}$ versus normalized stiffness of the patch.

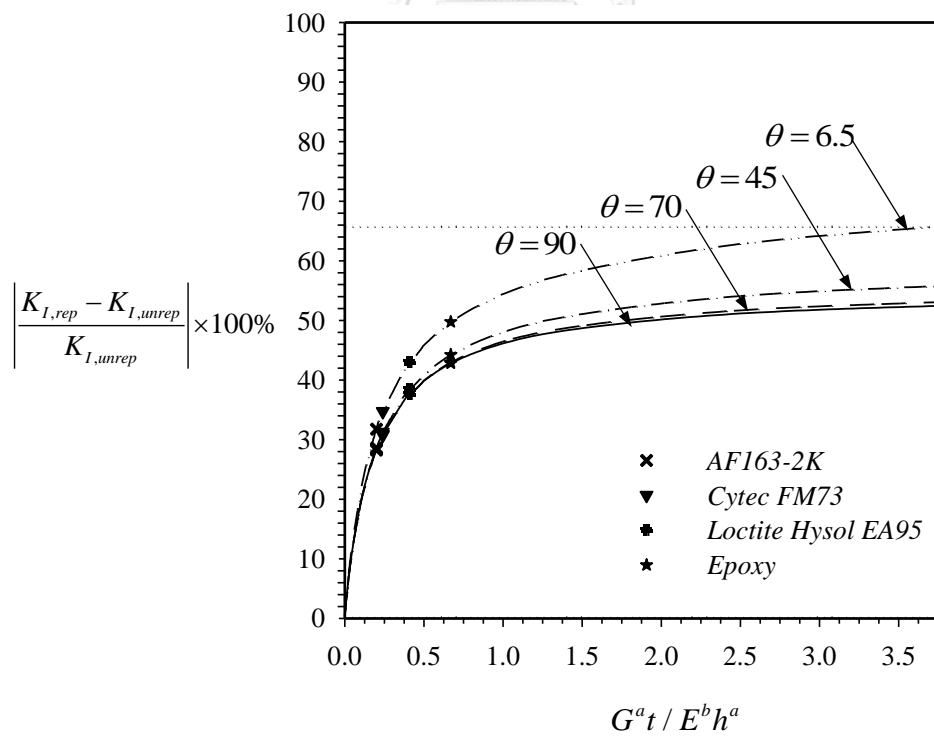


Figure 4.23. Percent reduction of mode-I SIF relative to unrepaired case at four selected points with $\theta \in \{6.5, 45, 70, 90\}$ versus normalized stiffness of adhesive layer.

4.2.3 Edge cracked bar

To additionally confirm the finding as pointed out in the previous two cases, consider, as a final example, the rectangular bar containing a through-the-thickness, surface-breaking crack as illustrated in Figure 4.14. The geometry of the cracked bar and the patch are taken as $w/t=0.75$, $h/t=0.875$, $a/t=0.5$, $d/t=0.2$ and $e/t=0.675$; the applied load is fixed; and properties of the material constituting the cracked bar are taken from Table 4.1.

The normalized mode-I stress intensity factors along the crack front of the cracked bar repaired by four different types of patches with properties shown in Table 4.2 are shown in Figure 4.24. The percent reduction of the mode-I stress intensity factor from the unrepaired case at four different points along the crack front (i.e., points associated with $s/t \in \{0, 0.25, 0.6, 0.967\}$) are reported as a function of the normalized stiffness of the patch $E^p h_p / E^b t$ and the normalized stiffness of the adhesive layer $G^a t / E^b h^a$ in Figures 4.25 and 4.26, respectively. As can be seen from this set of results, the same conclusion about the influence of the stiffness of the patch and the adhesive layer can be drawn. This piece of information can be potentially useful as the guideline in the selection of the patch and adhesive layer in the repair design.



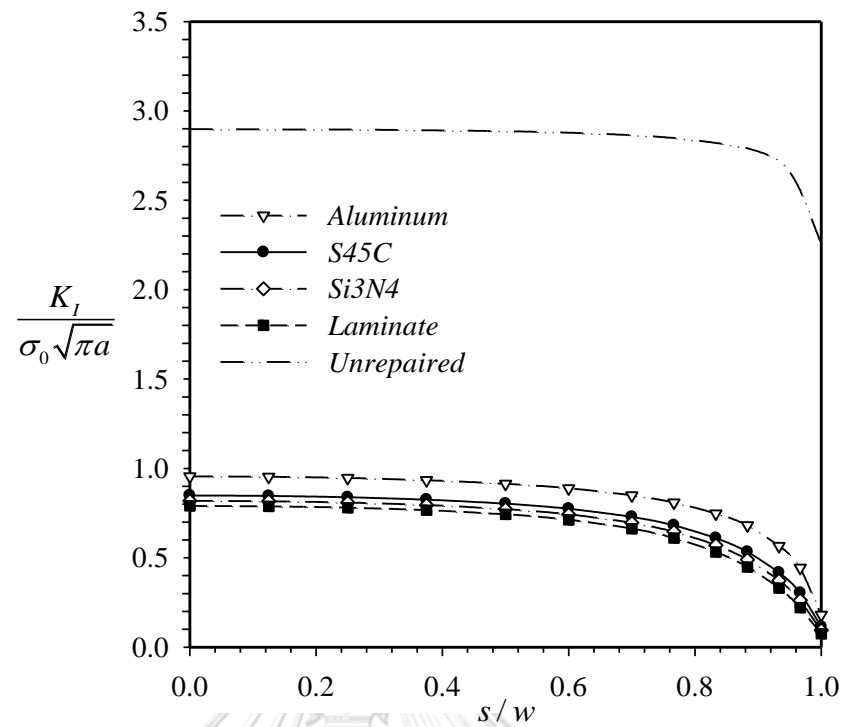


Figure 4.24. Normalized mode-I SIF along the crack front for edge cracked bar after repaired by four different types of patches.

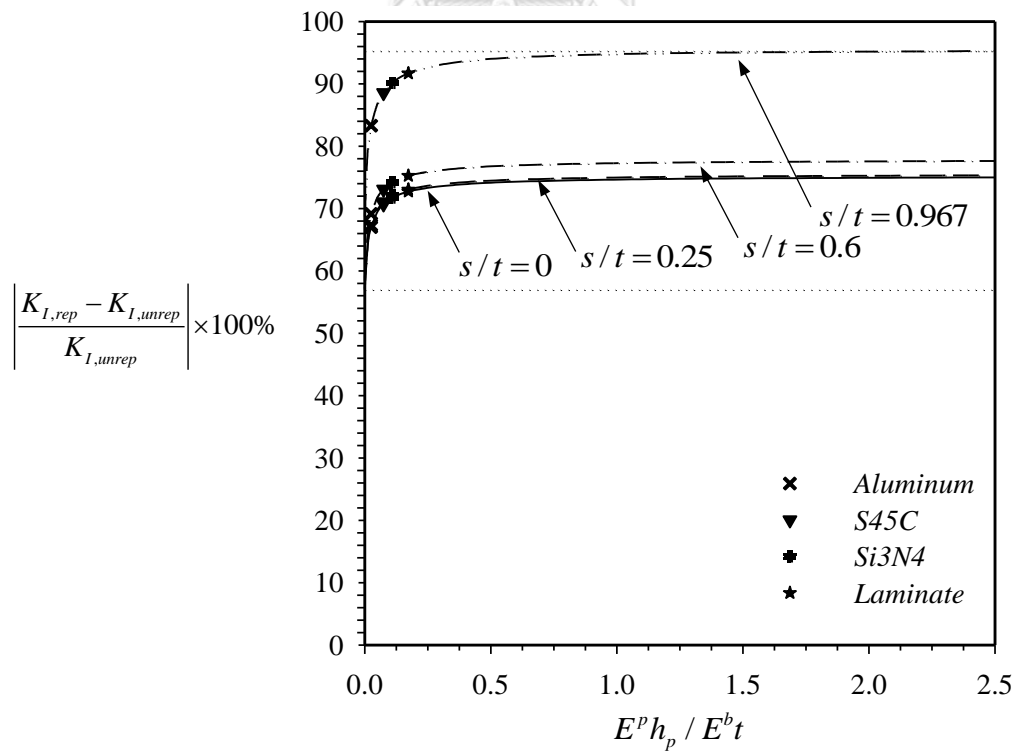


Figure 4.25. Percent reduction of mode-I SIF from unrepaired case at four selected points with $s/t \in \{0, 0.25, 0.6, 0.967\}$ versus normalized stiffness of the patch.

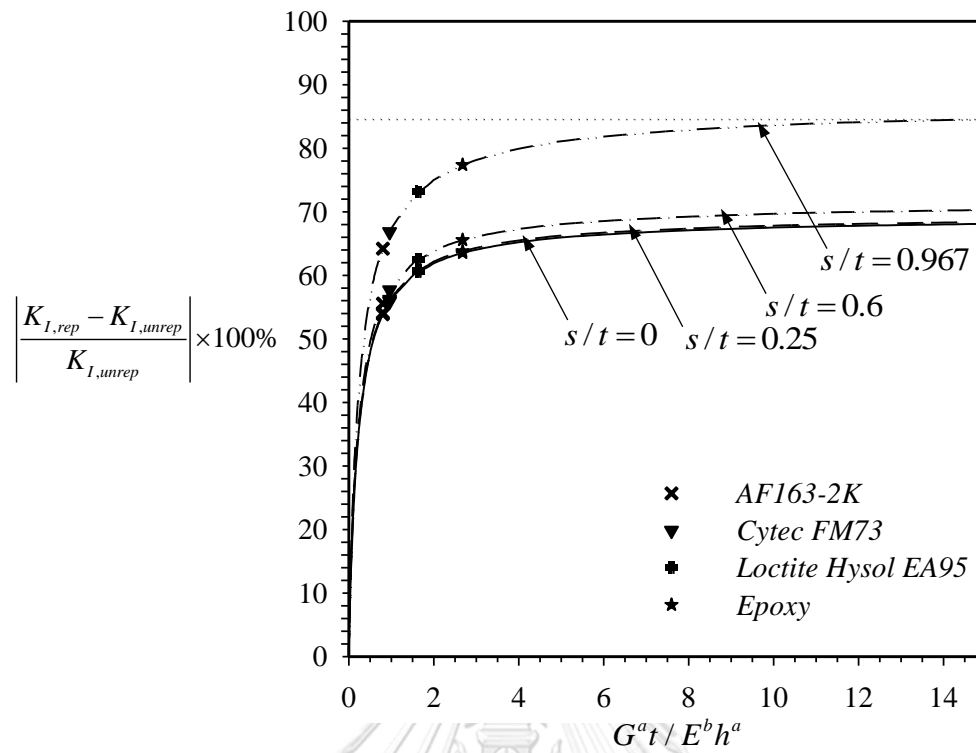


Figure 4.26. Percent reduction of mode-I SIF from unrepaired case at four selected points with $s/t \in \{0, 0.25, 0.6, 0.967\}$ versus normalized stiffness of adhesive layer.

CHAPTER 5

CONCLUSIONS AND REMARKS

The efficient and accurate BIE-FE coupling technique has been successfully implemented for the stress analysis of three-dimensional cracked bodies repaired by adhesively bonded patches. The boundary integral equation technique has been adopted to efficiently treat the cracked body whereas the standard finite element method has been utilized to tackle both the adhesive layers and the patches.

Results from a numerical study have indicated that numerical solutions accomplished from the proposed approach possess the good convergence behavior and are of excellent agreement with reliable benchmark solutions. The near-front approximation of the relative crack-face displacement has been enhanced by means of using special crack-tip elements and this allows relatively coarse meshes to be adopted in the discretization whereas still yielding sufficiently accurate fracture data along the crack front. Furthermore, the capability, versatility, and robustness of the current technique have been proved through the analysis of various problems including complex domains with multiple surface-breaking sides.

Results from the parametric study have indicated that as the Young's modulus of the patch (depending primarily on the types of the patches) increases, the stress intensity factors are reduced for the entire crack front for all cases investigated. In addition, the relative stiffness of both patches and adhesive layers has been found to play an important role on the reduction of the stress intensity factors along the crack front compared with those of the unrepaired case. Mainly, enhancing the stiffness of the patches and the adhesive layers gives rise to the increase in the percent reduction of the stress intensity factor from the unrepaired case. However, the enhancement of the patch stiffness to reduce the stress intensity factor is only effective for a certain limit. More specifically, increasing the patch stiffness beyond certain values or ranges may result in an insignificant change of the reduction of the stress intensity factor in the patching repair.

Results gained from the present study also provide the information essential as the guideline for the selection of both patches and adhesive layers not only to confine the stress intensity factors below the specified tolerance in order to prevent the subsequent crack growth but also to attain optimal repair design. In addition, as also pointed out in the previous chapter, the necessity of integrating the adhesive layer into the modeling depends mainly on the relative stiffness of the adhesive layer itself. For relatively high relative stiffness, ignorance of the adhesive layer in the mathematical model is recommended to save the computational cost. On the contrary, the integration of the adhesive layer in the modeling is obligatory and has the significant influence on the predicted stress intensity factor if its relative stiffness is relatively low.



The present work can be potentially and directly extended to incorporate both the bending and three-dimensional effects of the patches on the performance of the repair. In addition, integration of the material anisotropy of the patches, the nonlinear behavior of the adhesive material, and the non-planar repair surfaces are also of interest and requires nontrivial treatment.



REFERENCES



จุฬาลงกรณ์มหาวิทยาลัย
CHULALONGKORN UNIVERSITY

- Sangid MD. The physics of fatigue crack initiation. *International journal of fatigue*, 57, 58-72, 2013.
- Robert JD, and Justin MO. *Manual for repair and retrofit of fatigue cracks in steel bridges*. 2013.
- Mosallam AS, Bayraktar A, Elmikawi M, Pul S, Adanur S. Polymer Composites in Construction: An Overview. *SOJ Mater Sci Eng* 2 (1), 25, 2013.
- Zhu SP, Lei Q, Huang HZ, Yang YJ, Peng W. Mean stress effect correction in strain energy-based fatigue life prediction of metals. *International Journal of Damage Mechanics*, 26(8), 1219-1241, 2016.
- Arendt C and Sun CT. *Bending effects of unsymmetric adhesively bonded composite repairs on cracked aluminum panels*, 1994.
- Baker AA, Jones R. *Bonded repair of aircraft structures*. Dordrecht: Martinus Nijhoff, 1988.
- Jones R. *Bonded repair of damage*. *Journal of the Aeronautical Society of India*, 1984.
- Ratwani MM. *Characterization of Fatigue Crack Growth in Bonded Structures. Crack Growth Prediction in Bonded Structures*, volume 1, 1977a.
- Ratwani MM. *Characterization of Fatigue Crack Growth in Bonded Structures. Analysis of Cracked Bonded Structures*, volume 2, 1977b.
- Ratwani MM. A parametric study of fatigue crack growth behavior in adhesively bonded metallic structures. *Journal of Engineering Materials Technology*, 1978.
- Ratwani MM. *Analysis of cracked, adhesively bonded laminated structures*. *AIAA Journal*, vol 17(9), 988-994, 1979.
- Rose LRF. An application of the inclusion analogy for bonded reinforcements. *International Journal of Solids and Structures*, 17(8), pp. 827-838, 1981.
- Sun CT, Klug J, Arendt C. *Analysis of cracked aluminum plates repaired with bonded composite panels*. *AIAA Journal*, 34(2), pp. 369-74, 1996.

- Young A, Rooke DP, Cartwright DJ. Analysis of patched and stiffened cracked panels using the boundary element method. *International journal of solids and structures*, 29(17), pp. 2201-2216, 1992.
- Alaimo A, Milazzo A, Orlando C. Boundary elements analysis of adhesively bonded piezoelectric active repair. *Engineering fracture mechanics*, 76(4), pp. 500-511, 2009.
- Jiann-Quo T, Kam-Lun S. Analysis of cracked plates with a bonded patch. *Engineering Fracture Mechanics*, 40(6), pp. 1055-1065, 1991.
- Liu HB, Zhao XL, Al-Mahaidi R. Boundary element analysis of CFRP reinforced steel plates. *Composite Structures*, 91(1), pp. 74-83, 2009.
- Pisa CD, Aliabadi MH. Boundary element analysis of stiffened panels with repair patches. *Engineering Analysis with Boundary Elements*, 56, pp. 162-175, 2015.
- Salgado NK, Aliabadi MH. The application of the dual boundary element method to the analysis of cracked stiffened panels. *Engineering Fracture Mechanics*, 54(1), pp. 91-105, 1996.
- Salgado NK, Aliabadi MH. The boundary element analysis of cracked stiffened sheets, reinforced by adhesively bonded patches. *International journal for numerical methods in engineering*, 42(2), pp. 195-217, 1998.
- Sekine H, Yan B, Yasuho T. Numerical simulation study of fatigue crack growth behavior of cracked aluminum panels repaired with a FRP composite patch using combined BEM/FEM. *Engineering Fracture Mechanics*, 72(16), pp. 2549-2563, 2005.
- Useche J, Sollero P, Albuquerque EL, Palermo L. Boundary element analysis of cracked thick plates repaired with adhesively bonded composite patches. *SDHM: Structural Durability & Health Monitoring*, 4(2), pp. 107-115, 2008.
- Wen PH, Aliabadi MH, Young A. Stiffened cracked plates analysis by dual boundary element method. *International journal of fracture*, 106(3), pp. 245-258, 2000.
- Wen PH, Aliabadi MH, Young A. Boundary element analysis of flat cracked panels with adhesively bonded patches. *Engineering fracture mechanics*, 69(18), pp. 2129-2146, 2002.

- Wen PH, Aliabadi MH, Young A. Boundary element analysis of curved cracked panels with adhesively bonded patches. *International journal for numerical methods in engineering*, 58(1), pp. 43-61, 2003.
- Widagdo D, Aliabadi MH. Boundary element analysis of cracked panels repaired by mechanically fastened composite patches. *Engineering analysis with boundary elements*, 25(4-5), pp. 339-345, 2001.
- Yu QQ, Zhao XL, Chen T, Gu XL, Xiao ZG. Crack propagation prediction of CFRP retrofitted steel plates with different degrees of damage using BEM. *Thin-Walled Structures*, 82, pp. 145-158, 2014.
- Gurtin, Morton E. *Linear Theories of Elasticity and Thermoelasticity: Linear and Nonlinear Theories of Rods, Plates, and Shells. The Linear Theory of Elasticity*, pp. 1-295, 1973.
- Karasudhi P. *Foundations of solid mechanics*. Springer Science & Business Media, vol. 3, 2012.
- Timoshenko SP, Goodier JN. *Theory of elasticity-3rd ed*. McGraw-Hill, 1970.
- Rungamornrat J, Mear ME. A weakly-singular SGBEM for analysis of cracks in 3D anisotropic media. *Computer Methods in Applied Mechanics and Engineering*, 197(49-50), pp.4319-4332, 2008.
- Bathe KJ. *Finite element procedures-1st ed*, 2006.
- Hughes TJR. *The finite element method: linear static and dynamic finite element analysis*. Courier Corporation, 2012.
- Zienkiewicz OC, Taylor RL. *The finite element method: solid mechanics*, Butterworth-Heinemann, 2000.
- Li S, Mear ME, Xiao L. Symmetric weak-form integral equation method for three-dimensional fracture analysis. *Computer Methods in Applied Mechanics and Engineering*, 151(3-4), pp.435-459, 1998.
- Gutknecht, Martin H. Variants of BICGSTAB for matrices with complex spectrum. *SIAM journal on scientific computing*, 14(5), 1020-1033, 1993.

- Saad, Schultz MH. GMRES: A generalized minimal residual algorithm for solving nonsymmetric linear systems. *SIAM Journal on scientific and statistical computing*, 7(3), 856-869, 1986.
- Saad Y. *Iterative methods for sparse linear systems*. Siam, vol. 82, 2003.
- Van der Vorst HA. Bi-CGSTAB: A fast and smoothly converging variant of Bi-CG for the solution of nonsymmetric linear systems. *SIAM Journal on scientific and statistical computing*, 13(2), 631-644, 1992.
- Liu YJ, Xu N. Modeling of interface cracks in fiber-reinforced composites with the presence of interphases using the boundary element method. *Mechanics of Materials*, 32, 769–783, 2000.
- Ricci F, Franco F and Montefusco N. *Bonded Composite Patch Repairs on Cracked Aluminum Plates: Theory, Modeling and Experiments*. University of Naples “Federico II”, Department of Aerospace Engineering Italy, 2011.
- Rodríguez-Tembleque L and Aliabadi MH. Numerical simulation of fretting wear in fiber-reinforced composite materials. *Engineering Fracture Mechanics*, 168, 13-27, 2016.

VITA

NAME Binh Viet Pham

DATE OF BIRTH 12 January 1992

PLACE OF BIRTH Binh Thuan province, Vietnam.

INSTITUTIONS ATTENDED Faculty of Civil Engineering, Ho Chi Minh City University of Technology, Vietnam National University Ho Chi Minh City, 740128, Vietnam.

HOME ADDRESS Binh Thuan province, Vietnam.

AWARD RECEIVED

- Encouragement scholarship for excellent students of HCMUT in 2011, 2012, 2013 and 2014.
- Thanhnien daily newspaper's scholarship for excellent students in HCM city in 2014.
- Comprehensively excellent students in 2011 - 2012 and 2013 - 2014.